AN EXPERIMENTAL INVESTIGATION OF HYPERSONIC FLOW OVER BLUNT NOSED CONES AT A MACH NUMBER OF 5.8

Thesis by
William T. O'Bryant
Commander, U. S. Navy

In Partial Fulfillment of the Requirements
For the Degree of
Aeronautical Engineer

California Institute of Technology
Pasadena, California
1956

ACKNOWLEDGMENTS

The writer wishes to thank his advisor, Professor Lester Lees, for his suggestions, encouragement, and whole-hearted support throughout this investigation.

The author also wishes to express his sincere gratitude to the Naval Postgraduate School and the Bureau of Aeronautics of the Navy Department, whose interest, support, and policies made this graduate study possible.

Helpful suggestions and criticisms by other staff members, particularly Mr. J. M. Kendall, Mr. Robert E. Oliver, and Mr. Toshi Kubota are gratefully acknowledged.

To Mr. C. A. Bartsch and his co-workers, particularly Mr. George Carlson of the GALCIT Machine Shop, whose skill contributed to the successful fabrication of the models, and to the staff of the GALCIT 5 x 5 inch hypersonic wind tunnel for their help during the entire program, the writer is indebted.

A special mention is due to Mrs. Fae Kelley for her help in making the necessary computations and expert preparation of the curves for the final thesis copy. Sincere appreciation is extended to Mrs. G. Van Gieson who prepared the manuscript and supplied many helpful suggestions.

The writer finally wishes to thank his wife, Jane, for her enduring patience and encouragement which played an important part in the completion of this investigation. To her this thesis is dedicated.

ABSTRACT

Shock shapes were observed and static pressures were measured on spherically-blunted cones at a nominal Mach number of 5.8 over a range of Reynolds numbers per inch from 97,000 to 238,000 for angles of yaw from 0° to 8°. Six combinations of the bluntness ratios 0.4, 0.8, and 1.064 with the cone half angles 10°, 20°, and 40° were used in determining the significant parameters governing pressure distribution.

The pressure distribution on the spherical nose for both yawed and unyawed bodies is predicted quite accurately by the modified Newtonian theory given by $C_p = C_{p_{max}} \cos^2 \eta$, where η is the angle between the normal to a surface element and the flow direction ahead of the bow shock. On the nose-cone junction and the conical afterbody, cone half angle was found to be the significant parameter in determining the length of the transition zone. For a cone half-angle of 40°, a pressure minimum exists on the skirt immediately downstream of the nose-cone junction, but this pressure minimum is located far downstream when the half-angle is 20°. The tangent cone concept at angles of yaw is useful in predicting the downstream movement of the pressure minimum. Shock detachment distance between bow shock and body surface on the axis varies linearly with nose radius. Drag coefficients for bodies at zero yaw compare very closely with those obtained by integrating the modified Newtonian approximation, except at large half-angles and low bluntnesses where drag approaches that given by the Taylor-Maccoll theory for sharp cones.

TABLE OF CONTENTS

NOMENCLATURE

C_D	drag coefficient, dimensionless
C_{D_F}	foredrag pressure coefficient, dimensionless
C_p	pressure coefficient, $\dfrac{p - p_\infty}{\frac{1}{2}\rho_\infty U_\infty^2}$, dimensionless
$C_{p_{max}}$	pressure coefficient at the stagnation point, dimensionless
d	shock detachment distance, inches
$\bar{i}$	unit vector in the x- direction, dimensionless
$\bar{j}$	unit vector in the y- direction, dimensionless
$\bar{k}$	unit vector in the z- direction, dimensionless
M	Mach number, dimensionless
$\bar{n}$	unit vector normal to surface, dimensionless
p	air pressure, lb./sq. in.
q	dynamic pressure, lb./sq. in.
r	nose radius, inches
R	cone base radius, inches
R_e	Reynolds number, dimensionless
r/R	bluntness ratio, dimensionless
S	distance measured on the surface from the intersection of model surface with its longitudinal axis, inches
S/r	non-dimensional orifice distance
U	steam velocity, ft./sec.
x, y, z	a right hand system of coordinate axes, fixed in the body
α	yaw angle
γ	ratio of specific heats, dimensionless
∇	gradient

η	angle between free stream flow direction and the normal to the body surface
θ_c	cone half angle
ρ	air density, lb. sec.^{2}/ft.^{4}
σ	polar angle of spherical nose
ϕ	meridian angle

Subscripts

$(\ )_1$	static condition in front of bow shock wave
$(\ )_2$	static condition behind bow shock wave
$(\ )_\infty$	free stream conditions
$(\ )_o$	refers to stagnation, or reservoir conditions
$(\ )_j$	refers to nose-cone junction
$(\ )_{p.m.}$	at minimum pressure point
$(\ )_s$	static condition
$(\ )_{t_1}$	refers to total head in front of bow shock
$(\ )_{t_2}$	refers to total head behind bow shock

Superscripts

$(\ )'$	cone half angle of tangent cone

I. INTRODUCTION

Current interest in hypersonic flow over blunt nosed bodies has been generated by the realization that the effects of high recovery temperatures on present day materials force the use of blunt nosed missiles, not only to reduce the heat transfer rates, but also to provide the nose volume required by internal conduction, and by cooling or guidance apparatus. In addition to these considerations is the heartening fact that for a fixed body length or body volume, the nose shape producing minimum pressure foredrag is blunt. Eggers, Resnikoff, and Dennis (Ref. 1) show, for example, that for equal fineness ratios the drag of the 3/4- power body is as much as 20 per cent less than that of the cone over a range of Mach numbers from 2.73 to 6.28. Sommer and Stark (Ref. 2) show that for equal fineness ratios the drag of spherically blunted cones is less than that for cones over a range of Mach numbers from 1.2 to 7.0. This condition was shown to exist for bluntness ratios up to 12 per cent.

At hypersonic speeds the component of flight Mach number normal to the surface of a blunt body is much larger than unity, and the inertia forces predominate over the elastic forces in the disturbed air. But this condition is precisely that postulated by Newton in his original treatment of fluid motion, as pointed out in Reference 1. In Newton's theory the fluid is regarded as a collection of discrete particles with no interaction between particles. It admits no shock wave and hence fluid particles are unperturbed before striking the surface of a body moving through them. As each particle strikes the surface, it loses the component of its momentum normal to the body surface, while its tangential component is unchanged. The loss in normal momentum appears as an increase in pressure at the surface compared with the free stream pressure. The Newtonian pressure coefficient is

$$C_p = 2 \cos^2 \eta$$

where η is the angle between the free stream flow direction and the normal to the body surface. In the language of modern gas dynamics Newton's analysis applies strictly in the limiting case: $M \longrightarrow \infty$ and $\gamma \longrightarrow 1$.

Newtonian theory predicts a pressure coefficient at the stagnation point, $C_{p_{max}}$, equal to 2, but in a real gas the bow shock wave produces a finite volume compression and the rest of the deceleration to the stagnation point occurs isentropically. Therefore the actual value of $C_{p_{max}}$ is somewhat less than 2, being about 1.82 for $M_\infty = 5.8$ and $\gamma = 1.4$, and 1.66 at $M_\infty = 2$. As discussed by Lees (Ref. 3), Oliver (Ref. 4), and Penland (Ref. 5), the pressure distribution over a blunt body is predicted quite accurately if the Newtonian theory is modified by introducing the normalized pressure distribution

$$C_p/C_{p_{max}} = \cos^2 \eta$$

This result agrees exactly with the recent stagnation point theories of Ting-Yi Li (Ref. 6) and Hayes (Ref. 7).

Now the Newtonian approximation also predicts quite closely the value of the pressure on the surface of a semi-infinite unyawed circular cone, provided $M_\infty \sin \theta_c$ is sufficiently large. The object of the present investigation is to investigate experimentally the surface pressure distribution and shock wave shape in the intermediate region extending from the stagnation-point zone on a blunt nose to the end of a conical afterbody. Oliver (Ref. 4), in a recent study of a spherically-blunted 40° cone, observed an over-expansion below the final Taylor-Maccoll pressure value on the conical skirt, followed by a recompression to the proper asymptotic level. The present study seeks to determine what parameters are significant in determining the length of this transition zone, as well as other main features of the flow. It also extends the comparison with the Newtonian approximation and inviscid cone theories to the case of a yawed body.

Six models in the form of truncated circular cones with tangentially connected spherical nose segments were used to obtain static pressure measurements at angles of yaw of 0°, 4°, and 8°. The parameters which were varied were cone half angle, $\theta_c = 40^{\circ}$, 20°, and 10°; and bluntness ratio, or ratio of nose radius to cone base radius, $r/R = 0.4$, 0.8, and 1.064.

The tests were conducted at a nominal Mach number of 5.8 in the GALCIT 5 x 5 inch hypersonic wind tunnel. The experimental results presented in this report were obtained jointly with LT R. M. Machell, U. S. Navy.

II. EQUIPMENT AND PROCEDURE

A. Wind Tunnel

The tests were conducted in the GALCIT 5 x 5 inch hypersonic wind tunnel (leg no. 1), which is of the continuous-flow, closed-return type and can be operated with supply pressures between 1 and 6.7 atmospheres absolute. The Mach number was nominally 5.8. All tests were made at a fixed reservoir temperature of 225°F, over a range of reservoir pressures from 37 to 95 lbs. per sq. in. absolute. This temperature was selected to yield maximum Reynolds numbers per inch while insuring the absence of air condensation in the test section. A schematic diagram of the wind tunnel installation is shown in Figure 1. The test section, with one side plate removed, and two methods of model mounting are shown in Figure 2. An extensive description of the experimental facilities is given in Reference 8.

B. Models

The six truncated circular cones with tangentially connected spherical nose segments shown in Figure 3 were used in the investigation. They were constructed of brass and each had a base diameter of 1.75 inches. The parameters which were varied were the bluntness ratio, defined as the ratio of the nose to the base radius, r/R, and the cone half angle. The bluntness ratios used were 0.4, 0.8, and 1.064. The cone half angles used were 10, 20, and 40 degrees. Variation in these parameters caused model length to vary from .613 to 1.734 inches.

The models varied individually as follows:

MODEL SPECIFICATIONS

Model Number	1	2	3	4	5	6
Cone Half Angle, θ_c, (degrees)	40	40	20	20	20	10
Nose Radius (inches)	0.35	0.70	0.35	0.70	0.931	0.70
Bluntness Ratio, r/R	0.4	0.8	0.4	0.8	1.064	0.8
Model Length (inches)	0.849	0.654	1.731	1.057	0.613	1.631
Number Pressure Orifices	16	13	13	14	8	16

Note: Model number 5 was the limiting case where the spherical nose was the largest which could be inscribed within a 20° half-angle cone, and hence was merely a segment of a sphere.

Static pressure orifices on the front surfaces were .014 to .020 inches in diameter and were small enough to insure a pressure variation across the orifice diameter of less than five per cent of the stagnation pressure. (See Appendix for a discussion of accuracy.) Figure 4 shows the method of construction of a typical model. The axial orifice intersected a shaft which was drilled from the after end of the model sting. This shaft was subsequently plugged so that pressure would be transmitted through the metal tube inserted in the side of the sting. The number of orifices drilled in each model varied from eight to sixteen as shown in Figures 5 to 7, which also give orifice locations. The orifices were located on from four to eight rays depending on the particular model shape.

C. Model Mounting

The models were mounted in the test section in the region of most uniform flow conditions as determined by previously conducted static pressure calibration surveys. Distance from the nozzle throat was 24 inches when models were mounted on an axially driven support rod as shown in Figure 2A. The support rod itself was in turn supported at its upstream end by a vertically actuated strut which was at least 4.5 inches downstream of the model base. This method of mounting was used to test five models at zero angle of yaw. For yaw tests the models were mounted on two vertically actuated struts 3.875 inches apart as shown in Figure 2B. Distance from the nozzle throat was 22 inches and the most forward strut was 3.5 inches downstream of the model base. This method of mounting was used to test a sixth model at zero angle of yaw and two others at angles of yaw of 4 and 8 degrees as well as at zero yaw.

Model stings were designed to conform to the size least likely to affect static pressure readings according to Reference 9. For some models one or two pressure tubes on the base were positioned outside the circle of radius 0.7R, but these tubes had a negligible effect on the results.

Each model carried a close fitting collar-and-shaft type sting such that a collar screwed to the base of the model fitted over a shaft screwed to the model support, thus permitting rotation of the model about its longitudinal axis. A set-screw in the collar permitted the model to be locked in any desired rotational position. (Figure 4)

Saran tubing, a flexible plastic material, was attached to the steel tubes at the base of the model and was led to the outside of the tunnel through "o-ring" seals in a side port of the test section. Connections were there made to either silicone or mercury manometers, depending on expected pressures. The system was thoroughly leak-checked.

D. Test Procedure

1. Pressure Measurement

Reference 4 indicates the time required for temperature stabilization of model and test section is approximately $1\frac{1}{2}$ hours. Accordingly, the tunnel was operated for this length of time at the stagnation pressure desired for pressure measurement before readings were taken.

In order to minimize the effects of irregularities in flow direction occurring across the test section, the model was rotated upon its axis to three different positions 90 degrees apart during zero yaw tests, and pressures were read at each position. A similar procedure for minimizing flow irregularities was used in angle of yaw tests, except that a complete survey of pressures along each of the eight rays of the model was desired in addition. To accomplish both aims, the model was rotated to each of four positions 45 degrees apart, beginning with a ray in a vertical position. In each position the model nose was moved successively to angles of yaw of $+8^\circ$, $+4^\circ$, 0°, -4°, and -8° in the vertical plane, and pressures were taken at each angle. The use of minus angle of yaw positions reduced by half the number of times the model had to be rotated.

2. Tests

All six models were tested at zero angle of yaw at a stagnation pressure of 75 lbs. per sq. in. absolute. In order to ascertain Reynolds number effects, models 1 and 4 were tested at zero angle of yaw at varying stagnation pressures. Angle of yaw tests were also performed using models 1 and 4. These models were selected because they were completely dissimilar in the two geometrical parameters varied in this investigation. A summary of test conditions follows:

Model No.	Test Conditions			
	Vertical Yaw Angle (degrees)	p_o (psia)	Mach No.	Re/in. x 10^{-5}
1	0	75	5.8	1.91
	0	95	5.8	2.38
	4	95	5.8	2.38
	8	95	5.8	2.38
2	0	75	5.8	1.91
3	0	75	5.8	1.91
4	0	37	5.7	0.97
	0	54	5.7	1.41
	0	75	5.8	1.91
	0	95	5.8	2.38
	4	95	5.8	2.38
	8	95	5.8	2.38
5	0	75	5.8	1.91
6	0	75	5.8	1.91

III. RESULTS AND DISCUSSION

A. Schlieren Observations

Figures 8 through 13 are schlieren photographs of the six models at zero angle of yaw, at a nominal Mach number of 5.8. Figures 14 through 17 are photographs of models 1 and 4 at vertical angles of yaw of 4 and 8 degrees.

As in most hypersonic flows, the shock wave is fairly close to the body surface. The outstanding feature of the schlieren observations is the variation of shock shape with cone half-angle. Cone half-angles of 40° show a characteristic inflection point in the shock wave some distance downstream of the spherical nose portion of the model, but prior to the intersection with the first Mach wave from the model base.* (Figures 8 and 9) For small bluntness ratios the shock shape is dominated by the cone skirt, as shown in Figures 8 and 10. For large bluntness ratios, shock shape is dominated by the spherical nose as shown by Figure 9 and by Figures 11 through 13. These observations are true for any angle of yaw from 0° to 8°. However, angle of yaw produces some distortion in the curvature of the shock waves.

The ratio of measured detachment distance, d, between bow shock and body surface on the axis of revolution of the model at zero yaw, to model nose radius, r, is shown in the following table:

---

* See discussion of pressure distribution, page 12.

Model No.	d(in.)	r(in.)	d/r
1	0.0594	0.350	0.1695
2	0.1153	0.700	0.1649
3	0.0592	0.350	0.1692
4	0.1121	0.700	0.1602
5	0.1496	0.931	0.1607
6	0.1098	0.700	0.1569
	Average =		0.164

Thus, shock detachment varies nearly linearly with nose radius, as predicted theoretically. For instance, Ting-Yi Li (Ref. 6) predicts a value of $d/r = 0.137$ for $M_\infty = 5.8$ as given by

$$d/r = \frac{1}{\dfrac{(1 - \rho_1/\rho_2)^2}{\rho_1/\rho_2\left(1 - \sqrt{1 - (1 - \rho_1/\rho_2)^2}\right)} - 1}$$

where ρ_1/ρ_2 is the ratio of the density before a strong shock to that behind it. Hayes (Ref. 7) predicts a value of $d/r = 0.118$ for $M_\infty = 5.8$ as given by

$$d/r = \frac{\rho_1/\rho_2}{1 + \sqrt{2\,\rho_1/\rho_2}}$$

Both theories assume that $\rho_1/\rho_2 << 1$. Since $\rho_1/\rho_2 = 0.191$ for $M_\infty = 5.8$, and is not very small compared with unity, the agreement is considered to be good.

Heybey (Ref. 10) predicts a value of $d/r = 0.140$ for $M_\infty = 5.8$ which includes a correction for compressible flow behind the shock wave.

B. Surface Pressure Distribution

1. Unyawed Bodies

Surface pressure distributions for the six models at zero yaw are shown in Figures 18 through 23. Values of $C_p/C_{p_{max}}$ were obtained from observed data as explained in the Appendix. Both $C_p/C_{p_{max}}$ and the quantity $\cos^2 \eta$ appearing in the Newtonian approximation are plotted versus the non-dimensional orifice distance, S/r, where S is measured along the body surface from the intersection of the nose surface with the longitudinal axis. Taylor-Maccoll values of $C_p/C_{p_{max}}$ for a semi-infinite cone, as given by Kopal (Ref. 11), are also plotted over the conical portion of each model. In order to bring out the effect of bluntness ratio, r/R, with cone half angle held constant, the data of Figures 18 and 19 for $\theta_c = 40^\circ$ are replotted in Figure 24. Likewise the data of Figures 20 through 22 for $\theta_c = 20^\circ$ are replotted in Figure 25.

a. Spherical Nose

Close agreement between experimental pressures and Newtonian theory is evident on the spherical nose of each model. In each case, however, the test data fall slightly below the theory in the region of most rapidly changing pressure. The deviation is usually only a few per cent, in some instances approaching a maximum of only 10 per cent. In the region approaching the junction between the spherical nose and conical afterbody some models show a marked deviation associated with local effects.

b. Nose-Cone Junction and Conical Skirt

Examination of Figures 24 and 25 shows that bluntness ratio itself has very little effect on the surface pressure distribution and that the half-angle of the conical skirt is the dominant geometric parameter. A pressure minimum downstream of the nose-cone junction is found on the 40^{o} conical skirt, as in Oliver's tests, but this minimum moves a considerable distance aft when the cone half angle is reduced to 20^{o}. This behavior agrees with qualitative predictions based on previous theoretical studies of blunt bodies at hypersonic speeds. For large cone half-angles the pressure on the spherical nose just upstream of the nose-cone junction should be given very closely by the modified Newtonian approximation, because $M_{\infty} \sin \theta_{c} >> 1$. For example, at $M_{\infty} = 5.8$ and $\gamma = 1.4$, $C_{p_j} \cong 1.82 \sin^{2} \theta_{c}$. But the Taylor-Maccoll value of the pressure on the conical skirt far downstream is approximately $2.08 \sin^{2} \theta_{c}$ for $M_{\infty} \longrightarrow \infty$, * so that C_{p_j} <u>should lie below</u> this asymptotic value. Therefore one would expect to find a pressure minimum on the skirt for large cone half-angles, followed by a recompression to the Taylor-Maccoll value. This behavior should be accompanied by an inflection point in the bow shock wave as it adjusts itself to the Taylor-Maccoll conical shock angle far downstream. (Figure 8) Since the drag/length of the skirt is high the pressure minimum occurs relatively close to the nose-cone junction.

For smaller conical half angles the nose drag begins to dominate the flow pattern, and the surface pressure is expected to approach the

---

* At $M_{\infty} = 5.8$ the actual value is even higher.

monotonically-decreasing pressure distribution typical of the limiting case of a hemisphere-cylinder ($\theta_c = 0$) for $M_\infty > 3.50$ (air) as explained by Lees (Ref. 12). That such behavior does exist for hemisphere cylinders has been shown experimentally by many, see for example Oliver (Ref. 4). At $M_\infty = 5.8$ the pressures were shown to depart from Newtonian values on the spherical nose and consequently to be somewhat higher than Newtonian near the nose-cone junction. Figure 23 shows this behavior for $\theta_c = 10^\circ$. At the same time the skirt drag does not approach the nose drag until the skirt length is several nose diameters long. For both of these reasons the pressure minimum moves rapidly aft with decreasing θ_c. A critical value of the half-angle exists below which the pressure minimum no longer occurs. In these tests this angle was approximately 20°. It should be pointed out that this critical angle decreases with decreasing Mach number below 5.8, and for $M_\infty < 3.5$ (air), over-expansion occurs even on the hemisphere-cylinder.

Neglecting viscous effects, one would not expect the nose-skirt junction to influence the pressure upstream unless the Mach wave from the junction strikes the sonic line. At the junction the normal pressure gradient is discontinuous, and the corresponding discontinuity in pressure gradient along the surface is given by

$$\Delta \left(\frac{d\, C_p/C_{p_{max}}}{dS/r} \right) = + \frac{\gamma\ M^2}{\sqrt{M^2 - 1}} \left(\frac{C_p}{C_{p_{max}}} + \frac{2}{\gamma M_\infty^2} \frac{1}{C_{p_{max}}} \right)$$

For all the conditions of the present series of experiments this discontinuity in $\dfrac{d\, C_p/C_{p_{max}}}{d\, S/r}$

would reduce the negative surface pressure gradient, but would not reverse its sign. Now, examination of Figures 23 through 25 shows that the nose-cone junction influences the surface pressure upstream to an extent that cannot be explained by deviations from the Newtonian distribution. For example, the pressure coefficient at the junction is only 5 per cent above Newtonian for 40° cones, but is 37 per cent higher for 20° cones, and 146 per cent higher for 10° cones. The deviation can be explained, at least in part, by model surface irregularities which naturally occur at the nose-cone junction because of the difficulty in fabricating the desired "jump" in radius of curvature. Any gradual fairing in of the spherical nose with the conical skirt will reduce the negative surface pressure gradient on the nose and consequently raise the entire level of the downstream pressure distribution.

The data of Figures 18 and 21 and also Figures 24 and 25 do not show any significant Reynolds number effects over the range tested.

2. Yawed Bodies

Surface pressure distributions for models 1 and 4 at a yaw angle of 8° are shown in Figures 26 through 31. Both $C_p/C_{p_{max}}$ and the quantity $\cos^2 \eta$ are again plotted versus the non-dimensional orifice distance, S/r. The angle, η, in the yaw tests is no longer a simple function of body geometry, but is a function of angle of yaw as well. The angle was computed by the procedure given in the Appendix. To give adequate representation of the three-dimensional aspects introduced by yawed bodies, pressure distribution is plotted along four meridian planes. These planes are orientated as follows: (1) one plane is vertical; (2) two planes, referred to as diagonal meridian planes, lie in positions defined by the meridian angle ϕ, and are 45° and 315°

from the vertical meridian plane; (3) one plane is horizontal. Because of symmetry, the data obtained on the two diagonal planes have been averaged and plotted as for one plane. Likewise, the data obtained on the two halves of the horizontal plane have also been averaged and plotted for one half of the plane. Values of $C_p/C_{p_{max}}$ for a yawed cone, as given by the Stone-Kopal first order theory (Ref. 13), are also plotted over the conical portion of each model.

a. Spherical Nose

Yaw data show the same close agreement with the modified Newtonian approximation on the spherical nose as in the zero yaw case. In the region of most rapidly changing pressures, the experimental results again show slightly lower pressures than the theory. It is of importance to note at this point that in the yawed tests, except for the vertical meridian plane, the pressures obtained at orifices along a particular geometric ray are not pressure along one streamline, but are pressures obtained on many different streamlines. Hence, the modified Newtonian law holds over the entire surface in any direction for a spherical nose.

b. Nose-Cone Junction and Conical Skirt

In order to bring out the effects of yaw, the data of Figures 26 through 29 are replotted in Figure 32. Examination shows the downstream movement of the minimum pressure point as half angle is decreased. Here it is convenient to utilize a concept somewhat analogous to the tangent cone approximation. The upper and lower conical rays in the vertical meridian plane may be regarded at the various angles of yaw tested as belonging to two other cones at zero yaw whose half angles are given by the relations,

$$\theta_c' = \theta_c + \alpha \qquad \text{(Lower half plane)}$$

$$\theta_c' = \theta_c - \alpha \qquad \text{(Upper half plane)}$$

For the two models, then, four cones may be considered whose half angles are 12°, 28°, 32°, and 48°. It may be presumed that the 28° cone, represented in the lower half meridian plane of model 4, would have a minimum pressure point were its skirt to be sufficiently increased in length, since its pressures lie below the Stone-Kopal values on the cone. On the other hand the pressure distribution over the 12° tangent cone, being above the Stone-Kopal values, behaves very similarly to that given by the 10° cone of Figure 23. The yaw data confirm the zero yaw result in that the critical value of θ_c, below which there is no minimum pressure point, lies between a half angle of 28° and 12°.

Further evidence of the downstream movement of the pressure minimum as θ_c is decreased is revealed by Figure 33 which shows data for the vertical meridian plane of model 1 at angles of yaw of 0°, 4°, and 8°. The tangent cones have values of θ_c = 32°, 36°, 40°, 44°, and 48°. The location of the pressure minimum point downstream of the nose-cone junction in numbers of nose radii for various cone half angles is summarized in the table following:

θ_c or θ_c'	$(S/r)_{p.m.} - (S/r)_j$
48°	0.06
44°	0.09
40°	0.15
36°	0.25
32°	0.40
20°	2.28

Yaw tests show again that the nose-cone junction influences the surface pressure upstream to an unexplained but qualitatively predictable extent as half angle is varied. Per cent deviations of pressure coefficients from Newtonian values for actual and tangent cones as obtained from Figures 23 through 25 and from Figure 32 are summarized in the following table:

Model No.	θ_c or θ_c' (degrees)	Deviation from Newtonian (per cent)
6	10	146
4	12	133
4	20	37
4	28	17
1	32	10
1	40	5
1	48	10

When the cone skirt is sufficiently long the data show that the pressures approach the tangent cone values more closely than the values given by the Stone-Kopal first-order theory. Also shown in Figure 33 is the fact that $\left(\frac{C_p}{C_{p_{max}}}\right)-\left(\frac{C_p}{C_{p_{max}}}\right)_{\alpha=0}$ varies linearly over the range of yaw angles tested.

Variation of $C_p/C_{p_{max}}$ with variation in meridian angle is shown in Figure 34 as replotted from Figures 26 through 28.

C. Drag

By integrating the modified Newtonian approximation $C_p/C_{p_{max}} = \cos^2 \eta$ over the body surface, the following expression for drag coefficient at zero yaw is obtained for a spherically blunted cone:

$$C_D = C_{p_{max}} \left[\frac{1}{2} \cos^4 \theta_c \left(\frac{r}{R} \right)^2 + \sin^2 \theta_c \right]$$

In Figure 35 drag coefficients obtained by graphical integration of the experimental pressure distributions for the six models at zero yaw are compared with the theoretical value. The Taylor-Maccoll values for sharp cones are also shown.

Examination clearly shows the close agreement with the modified Newtonian approximation. However, at high half-angles and low bluntness ratios, the drag approaches that given by the Taylor-Maccoll theory.

IV. CONCLUSIONS

The results of this investigation provide the following conclusions regarding surface pressure distribution and shock wave shape for spherical nosed cones at a nominal Mach number of 5.8:

(1) Static pressure distribution on the spherical nose agrees very closely with the modified Newtonian theory over the range of α from 0° to 8°, of θ_c from 10° ro 40°, of r/R from 0.4 to 1.064, and of Reynolds number per inch from 97,000 to 238,000.

(2) Under all conditions of the present investigation the half angle of the conical skirt is the dominant geometric parameter by which pressure distribution over the nose-cone junction and the conical afterbody may be predicted, while bluntness ratio itself has very little effect.

(3) There is a critical cone half angle, θ_c, above which there exists a pressure minimum on the conical skirt. This pressure minimum is far downstream for low θ_c and moves toward the nose cone junction as θ_c increases. The critical θ_c for $M_\infty = 5.8$ is about 20°, and the pressure minimum moves from a point 2.28 times the nose radius downstream of the nose-cone junction for $\theta_c = 20^\circ$ to a point only .06 times the nose radius downstream of the junction for $\theta_c = 48^\circ$.

(4) At zero yaw the pressure on sufficiently long cone skirts approaches quite closely that given by the Taylor-Maccoll theory.

(5) At angles of yaw pressure distribution on sufficiently long cone skirts approaches quite closely that given by the Taylor-Maccoll theory as applied to tangent cones. The Stone-Kopal first order theory for yawed cones predicts the pressure behavior less accurately.

(6) $\left(\frac{C_p}{C_{p_{max}}}\right) - \left(\frac{C_p}{C_{p_{max}}}\right)_{\alpha=0}$ varies linearly with variation in angle of yaw in the range from 0° to 8°.

(7) There are no significant Reynolds number effects over the range of α, θ_c, r/R and R_e tested.

(8) Bow shock detachment distance on the model longitudinal axis varies linearly with model nose radius. The ratio of detachment distance to nose radius is found to be 0.164 as compared with the predictions of Li, Hayes, and Heybey which are 0.137, 0.118, and 0.140, respectively.

(9) For θ_c sufficiently large, and hence for a minimum pressure point sufficiently near the nose cone junction, an inflection point in the bow shock wave occurs.

(10) For low bluntness ratios shock shape is dominated by the conical afterbody, while for high bluntness ratios, shock shape is dominated by the spherical nose.

REFERENCES

1. Eggers, A. J., Jr.; Resnikoff, Meyer M.; and Dennis, David H.: Bodies of Revolution Having Minimum Drag at High Supersonic Airspeeds. National Advisory Committee for Aeronautics, Technical Note 3666, February, 1956.

2. Sommer, Simon C.; and Stark, James A.: The Effect of Bluntness on the Drag of Spherical-Tipped Truncated Cones of Fineness Ratio 3 at Mach Numbers 1.2 to 7.4. National Advisory Committee for Aeronautics, R. M. A52B13, April 25, 1952.

3. Lees, Lester: Hypersonic Flow. Institute of the Aeronautical Sciences, Preprint No. 554, June, 1955.

4. Oliver, Robert E.: An Experimental Investigation of Flow over Simple Blunt Bodies at a Nominal Mach Number of 5.8. GALCIT Hypersonic Wind Tunnel Memorandum No. 26, June 1, 1955. Also, J. of the Aero. Sci., Vol. 23, No. 2, February, 1956.

5. Penland, Jim A.: Aerodynamic Characteristics of a Circular Cylinder at Mach Number 6.86 and Angles of Attack up to 90°. National Advisory Committee for Aeronautics, R. M. L54A14, March 11, 1954.

6. Li, Ting-Yi and Geiger, R. E.: Stagnation Point of a Blunt Body in Hypersonic Flow. Institute of the Aeronautical Sciences, Preprint No. 629, January, 1956.

7. Hayes, W. D.: Some Aspects of Hypersonic Flow. Ramo-Wooldridge Corporation, January, 1955.

8. Eimer, M.: Direct Measurement of Laminar Skin Friction at Hypersonic Speeds. GALCIT Hypersonic Wind Tunnel Memorandum No. 16, July 1, 1953.

9. Harkins, W. D.: Base Pressure and Static Pressure for a Cone-Cylinder at a Nominal Mach Number of 5.8. GALCIT Hypersonic Wind Tunnel Memorandum No. 19, July, 1954.

10. Heybey, W. H.; Shock Distance in Front of Symmetrical Bodies. NAVORD Report 3594, December, 1953.

11. Staff of the Computing Section, Center of Analysis, Mass. Inst. of Technology, under direction of Zdenek Kopal: Tables of Supersonic Flow around Cones. Technical Report No. 1, 1947.

12. Lees, Lester: Inviscid Hypersonic Flow over Blunt-Nosed Slender Bodies. GALCIT Hypersonic Wind Tunnel Memorandum No. 31, February 1, 1956.

13. Staff of the Computing Section, Center of Analysis, Mass. Inst. of Technology, under direction of Zdenek Kopal: Tables of Supersonic Flow around Yawing Cones. Technical Report No. 3, 1947.

14. Ames Research Staff: Equations, Tables, and Charts for Compressible Flow. National Advisory Committee for Aeronautics, Report 1135, 1953.

APPENDIX

A. Computation of $C_p/C_{p_{max}}$ at Zero Yaw

Manometer values of static pressure were subtracted from manometer reference pressures to give static pressure at each orifice in cm Si or cm Hg. Since both silicone and mercury manometers were vacuum-referenced, the pressures were then corrected by the amount the vacuum differed from zero pressure absolute. Then all silicone pressures were converted to cm of mercury at existing room temperatures, giving static pressure p_s. The pressure at the stagnation orifice is assumed to be the total pressure behind the bow shock wave, p_{t_2}. To get free stream total pressure, p_{t_1}, the static pressure one inch upstream of the throat was converted from lbs. per sq. in. gage to cm of mercury and the barometric pressure was applied. The ratio p_{t_2}/p_{t_1} was used to enter Reference 14 to obtain M_∞ and p_1/p_{t_1}. The latter value, when multiplied by p_{t_1}, gave p_1, the free stream static pressure. Thus the ratio $C_p/C_{p_{max}}$ was obtained as follows:

$$C_p = \frac{\Delta p}{q_\infty} = \frac{p_s - p_1}{q_\infty}$$

$$C_{p_{max}} = \frac{p_{t_2} - p_1}{q_\infty}$$

and

$$C_p/C_{p_{max}} = \frac{p_s - p_1}{p_{t_2} - p_1}$$

B. Computation of $C_p/C_{p_{max}}$ at Angles of Yaw

At angles of yaw, no orifice was located at the stagnation point from which p_{t_2} could be found. p_{t_2} was obtained by using the pressure at the nose orifice with the model at zero angle of yaw and assuming that this value remained unchanged at angle of yaw. Since the model could be quickly altered in angle of yaw without changing tunnel conditions, the assumption is a valid one.

C. Computation of $\cos^2 \eta$ at Zero Yaw

The angle, η, is defined as the angle between the free stream flow direction and the normal to the surface at any point in question. Knowing the location of each orifice permits the determination of η and hence $\cos^2 \eta$.

D. Computation of $\cos^2 \eta$ at Angles of Yaw

The angle, η, is a function of the angle of yaw as well as of a function of surface geometry. The spherical nose and the cone skirt are treated separately.

The equation of a sphere in rectangular coordinates where the origin of the axes is at the center of the sphere is given by:

$$f = x^2 + y^2 + z^2 - r^2 = 0$$

The unit vector normal to the sphere is defined as the quotient of the gradient of the surface and the absolute value of the gradient. Hence,

$$\bar{n} = \frac{\nabla f}{|\nabla f|}$$

where $\nabla f = \bar{i}\ 2x + \bar{j}\ 2y + \bar{k}\ 2z$

and

$$|\nabla f| = 2\,(x^2 + y^2 + z^2)^{\frac{1}{2}}$$

Therefore,

$$\bar{n} = \frac{\bar{i}x + \bar{j}y + \bar{k}z}{r}$$

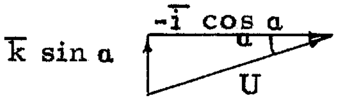

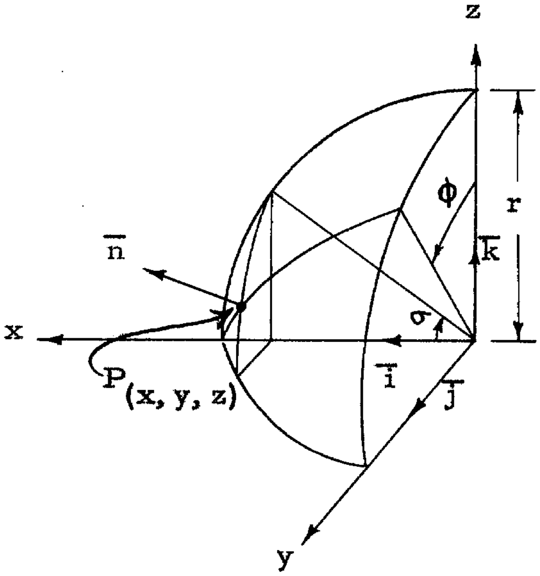

From the sketch the following quantities are defined:

α ≡ angle of yaw in the z- plane

σ ≡ polar angle measured from the x- axis

ϕ ≡ meridian angle measured counterclockwise on the base of spherical nose segment from the vertical z- axis

Any point on the surface is defined by the coordinates where

$$x = r\cos\sigma$$

$$y = r\sin\sigma\sin\phi$$

$$z = r\sin\sigma\cos\phi$$

The angle of yaw in the z- plane is given by

$$\bar{\alpha} = -\bar{i}\cos\alpha + \bar{k}\sin\alpha$$

Then $\cos\eta$ is defined as

$$\cos\eta = -\bar{n} \circ \bar{\alpha}$$

where $-\bar{n}$ is the inner unit normal at any point, P.

Hence,

$$\cos\eta = -\bar{n} \circ \bar{\alpha} = -\sin\alpha\sin\sigma\cos\phi + \cos\alpha\cos\sigma$$

The equation of the cone is

$$f_1 = x^2\tan\theta_c - y^2 - z^2 = 0$$

where θ_c is the cone half angle.

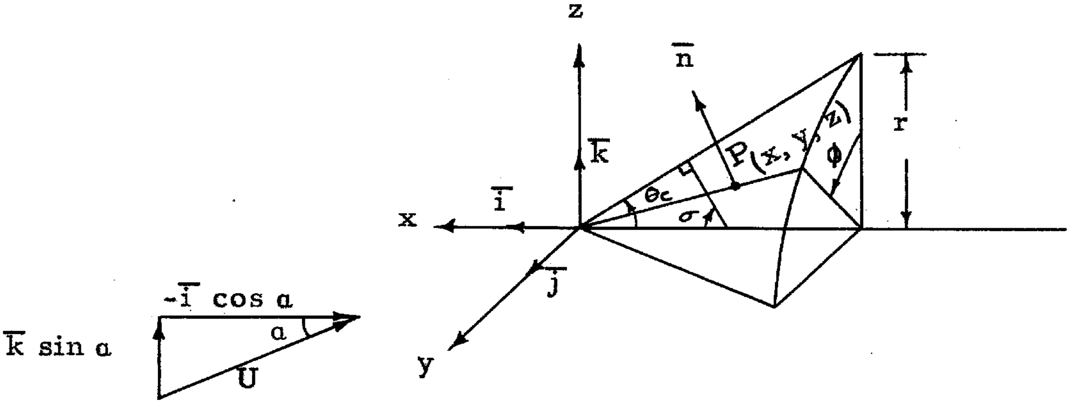

From the sketch, any point, P, on the surface is defined by the coordinates where

$$r = -x\tan\theta_c$$

$$y = r\sin\phi$$

$$z = r \cos \phi$$
$$y/x = - \sin \phi \tan \theta_c$$
$$z/x = - \cos \phi \tan \theta_c$$

From which

$$\bar{n} = \frac{\nabla f_1}{|\nabla f_1|} = \frac{2(\bar{i}\, x \tan^2 \theta_c - \bar{j} y - \bar{k} z)}{2(x^2 \tan^4 \theta_c + y^2 + z^2)^{\frac{1}{2}}}$$

$$\bar{n} = \frac{\bar{i} x \tan^2 \theta_c - \bar{j} y - \bar{k} z}{x \tan \theta_c \sec \theta_c}$$

$$\bar{n} = \bar{i} \sin \theta_c + \bar{j} \cos \theta_c \sin \phi + \bar{k} \cos \theta_c \cos \phi$$

Hence,

$$\cos \eta = - \bar{n} \circ \bar{\alpha} = - \cos \theta_c \cos \phi \sin \alpha + \sin \theta_c \cos \alpha$$

where

$$\sigma = \frac{\pi}{2} - \theta_c$$

at the junction of the spherical segment and the cone.

E. Accuracy Considerations

1. Measured Quantities

The following is a list of possible sources of error in the measured static pressure, p_s, and reservoir pressure, p_{t_1}:

(1) Reading errors

(2) Orifice diameter

(3) Orifice location errors

(4) Angle of yaw errors

(5) Meridian angle errors

The maximum random manometer reading error was estimated to be ± 0.3 per cent of the stagnation pressure for a reservoir pressure of 80 lbs. per sq. in. gage. Orifice diameter was designed to give a maximum pressure variation from the mean of ± 2.5 per cent of the stagnation pressure. However, it is assumed that pressure transmitted to the manometer varied by a negligible amount from the mean pressure across the orifice. Deviations from designed orifice positions were such as to produce errors no larger than ± 0.5 per cent of stagnation pressure. Errors caused by angle of yaw and meridian angle setting errors were negligible.

a. Static pressure, p_s

Total error in p_s is given as follows:

Reading error	± 0.3 per cent
Orifice size	± 0.0 per cent
Variation in orifice position	± 0.5 per cent
Total error in p_s	± 0.8 per cent

b. Reservoir pressure, p_{t_1}

The maximum error in reading the correct value of reservoir pressure was ± 0.5 per cent of stagnation pressure.

2. Computed Quantities

As the result of errors in measurements, the computed quantities had errors as follows:

$p_\infty = \pm 0.03$ per cent of stagnation pressure

$M_\infty = \pm 0.01$

3. Plotted Quantities

As the result of the errors noted above, the plotted values of $C_p/C_{p_{max}}$ contained maximum errors as follows:

Region of Model	Model No.	Fraction of $C_p/C_{p_{max}}$
Nose to $S/R \cong 0.2$	all	$< \pm 0.01$
$S/r \cong 0.2$ to nose-cone junction	1, 3	± 0.012
$s/r \cong 0.2$ to nose-cone junction	2, 4, 5, 6	± 0.01
Cone skirt	all	$< \pm 0.01$

LIST OF FIGURES

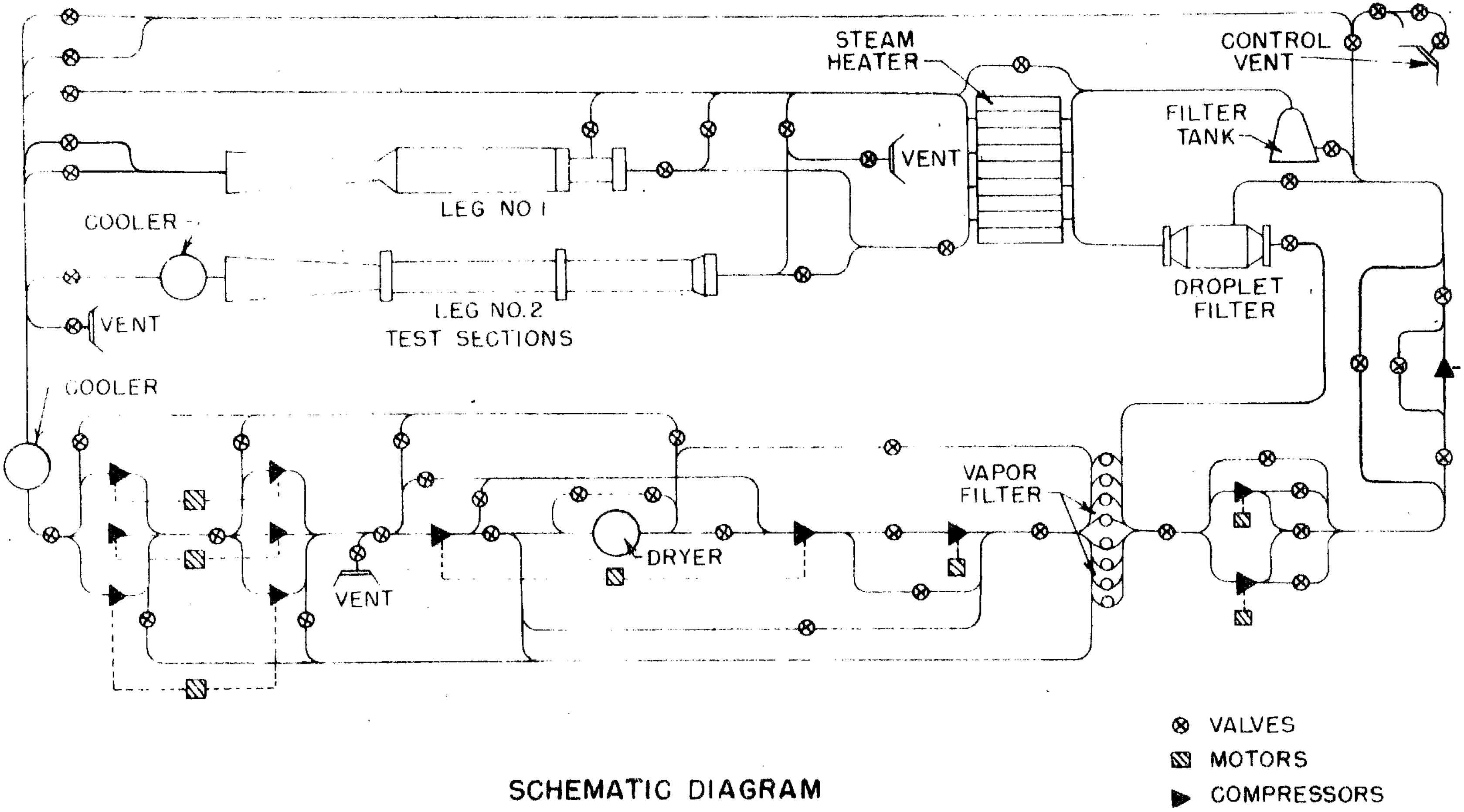

SCHEMATIC DIAGRAM

OF GALCIT 5x5in. HYPERSONIC WIND TUNNEL INSTALLATION

FIG. I

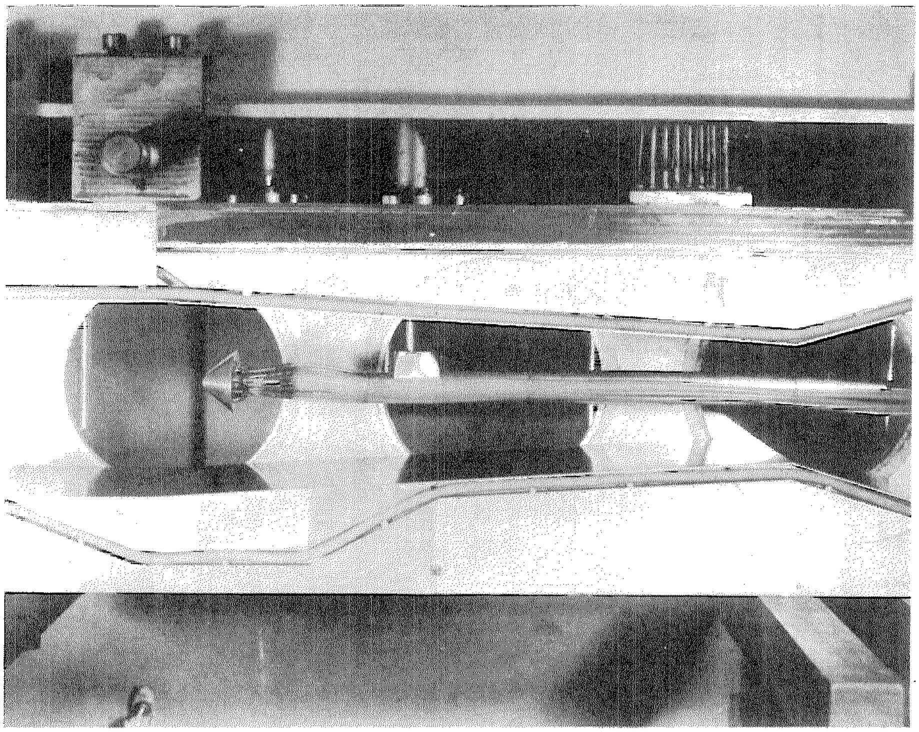

(A)

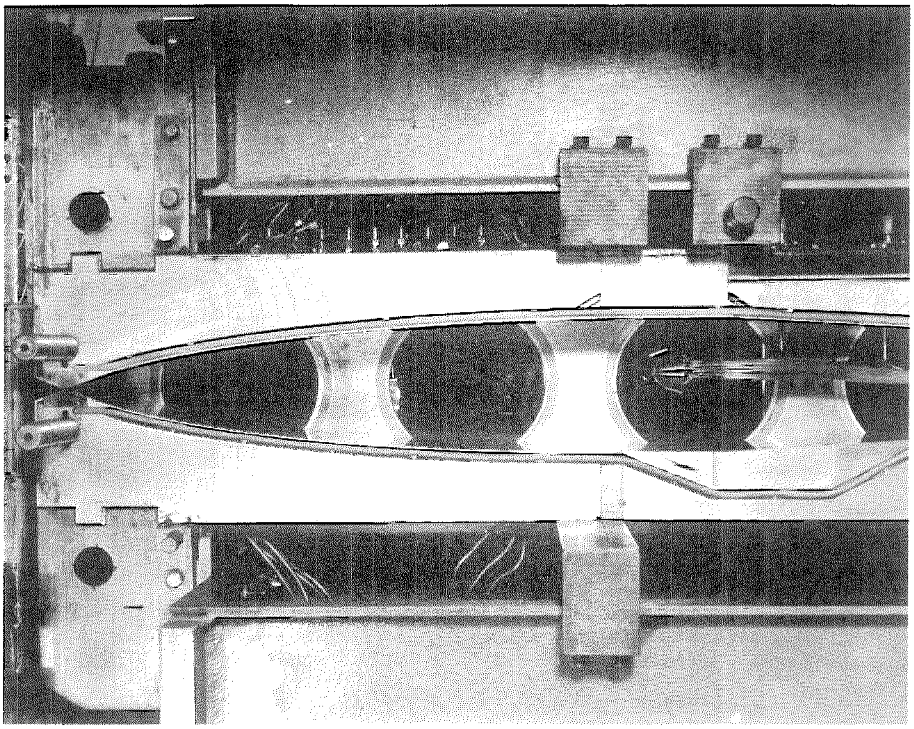

(B)

FIG. 2

TEST SECTION OF HYPERSONIC TUNNEL

SHOWING METHODS OF MOUNTING MODELS

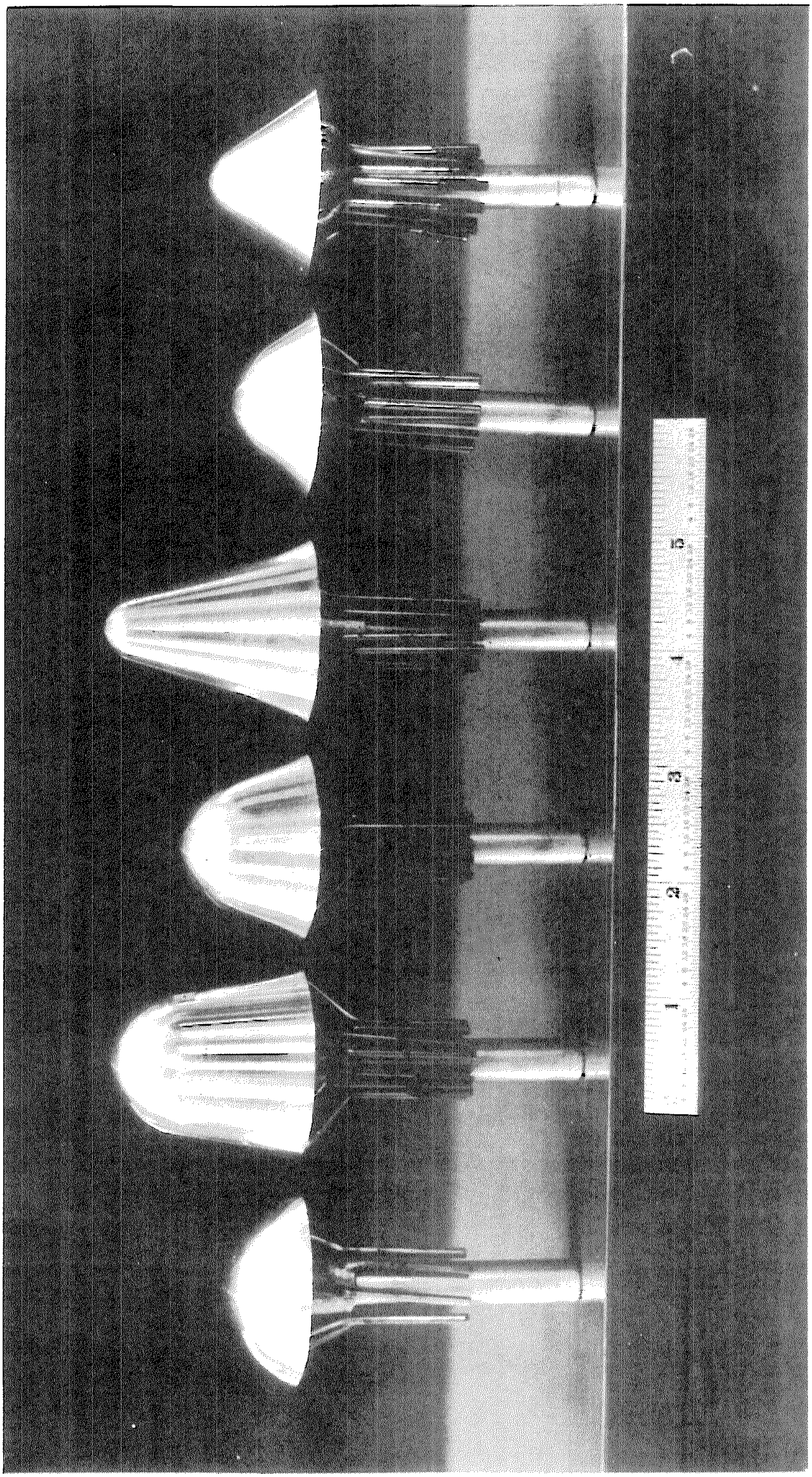

FIG. 3

SPHERICAL NOSED CONE STATIC PRESSURE MODELS

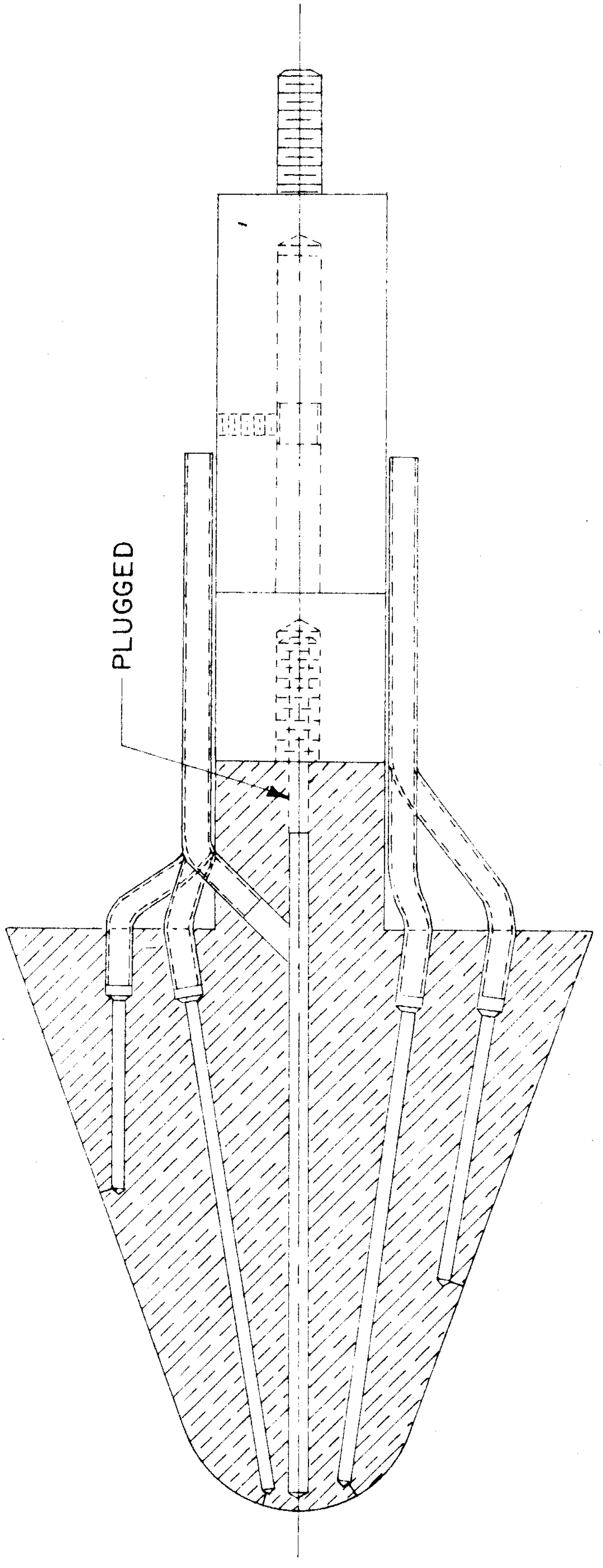

FIG. 4 DETAILS OF TYPICAL MODEL CONSTRUCTION

Orifice	S(in.)
1	0
2	0.070
3	0.105
4	0.140
5	0.210
6	0.210
7	0.280
8	0.315
9	0.350
10	0.385
11	0.420
12	0.490
13	0.630
14	0.805
15	0.980
16	1.155

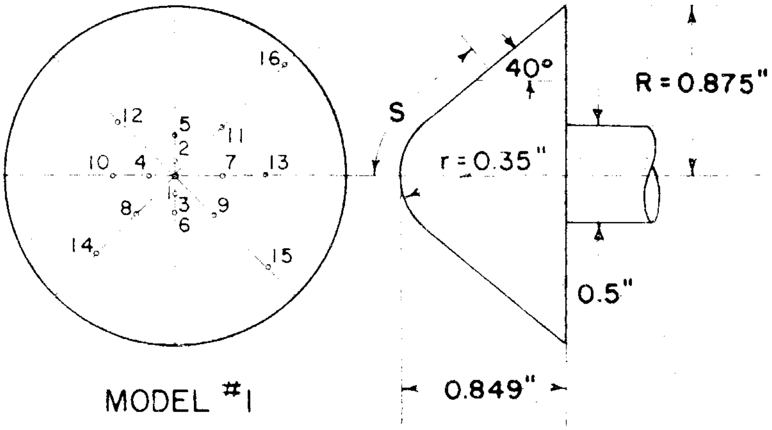

(A) 40° HALF ANGLE CONE

r/R = 0.4

Orifice	S(in.)
1	0
2	0.070
3	0.140
4	0.210
5	0.280
6	0.420
7	0.420
8	0.560
9	0.630
10	0.700
11	0.770
12	0.840
13	0.980

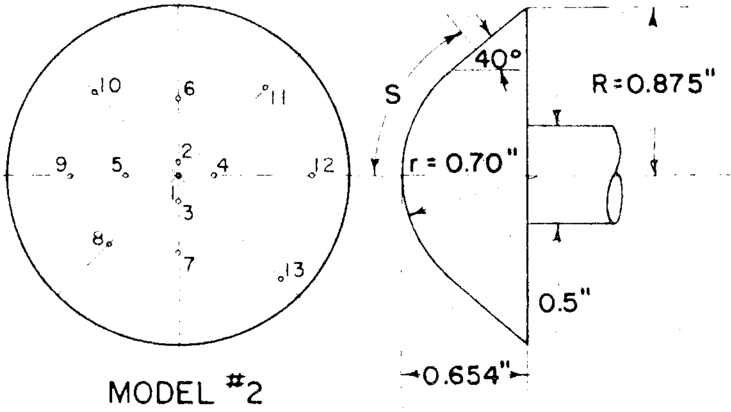

(B) 40° HALF ANGLE CONE

r/R = 0.8

FIG. 5

Orifice	S(in.)
1	0
2	0.105
3	0.175
4	0.280
5	0.385
6	0.490
7	0.595
8	0.735
9	0.735
10	0.875
11	1.155
12	1.435
13	1.715

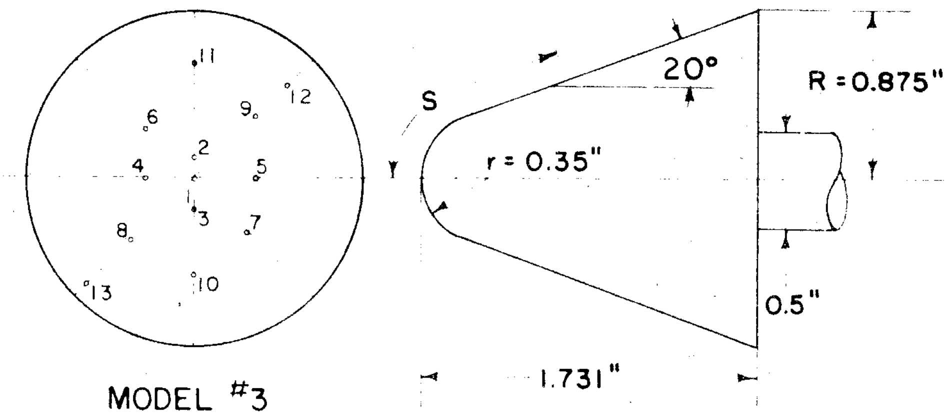

(A) 20° HALF ANGLE CONE
r/R = 0.4

Orifice	S(in.)
1	0
2	0.070
3	0.140
4	0.210
5	0.280
6	0.490
7	0.490
8	0.700
9	0.840
10	0.910
11	0.980
12	1.050
13	1.120
14	1.260

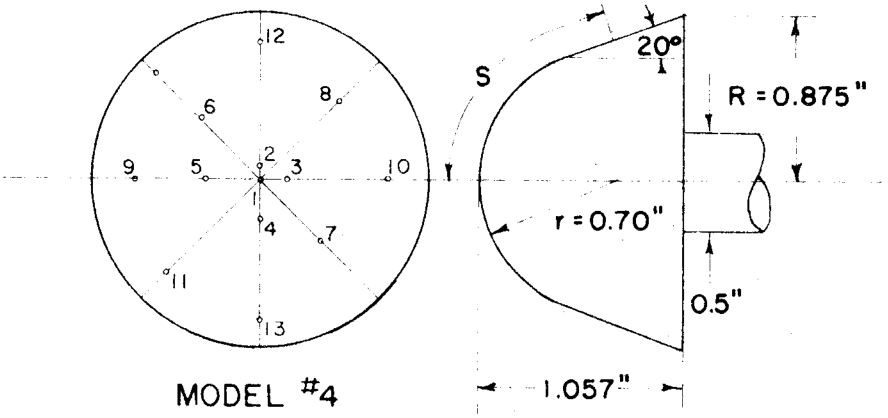

(B) 20° HALF ANGLE CONE
r/R = 0.8

FIG. 6

Orifice	S(in.)
1	0
2	0.093
3	0.186
4	0.279
5	0.372
6	0.650
7	0.650
8	0.931

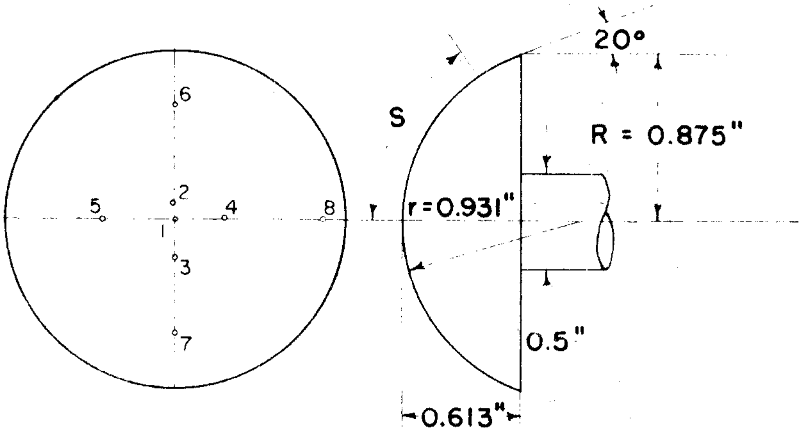

MODEL #5

(A) 20° SPHERICAL SEGMENT

$r/R = 1.064$

Orifice	S(in.)
1	0
2	0.070
3	0.140
4	0.210
5	0.338
6	0.420
7	0.420
8	0.630
9	0.840
10	0.910
11	0.980
12	1.050
13	1.120
14	1.260
15	1.540
16	1.820

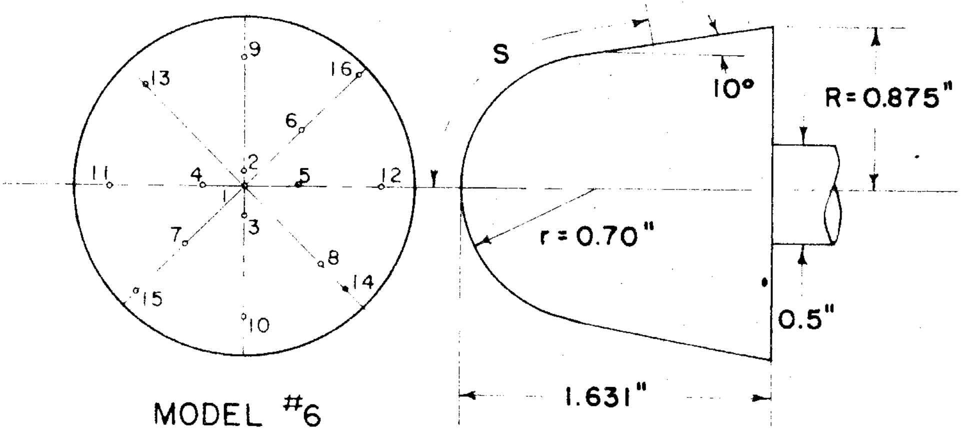

MODEL #6

(B) 10° HALF ANGLE CONE

$r/R = 0.8$

FIG. 7

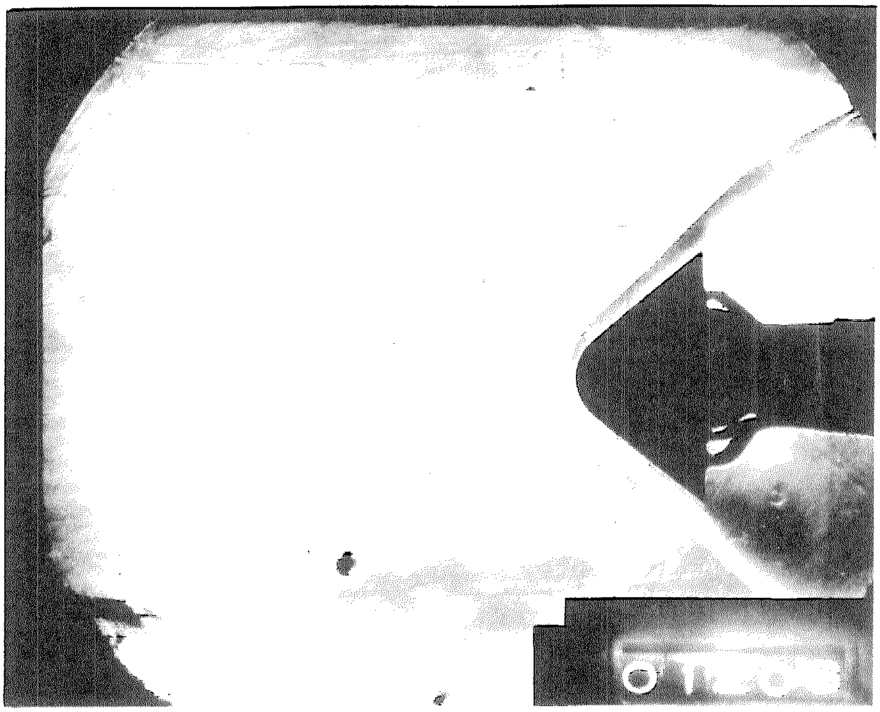

FIG. 8

SCHLIEREN PHOTOGRAPH OF 40° HALF ANGLE CONE

$r/R = 0.4$, $\alpha = 0^\circ$

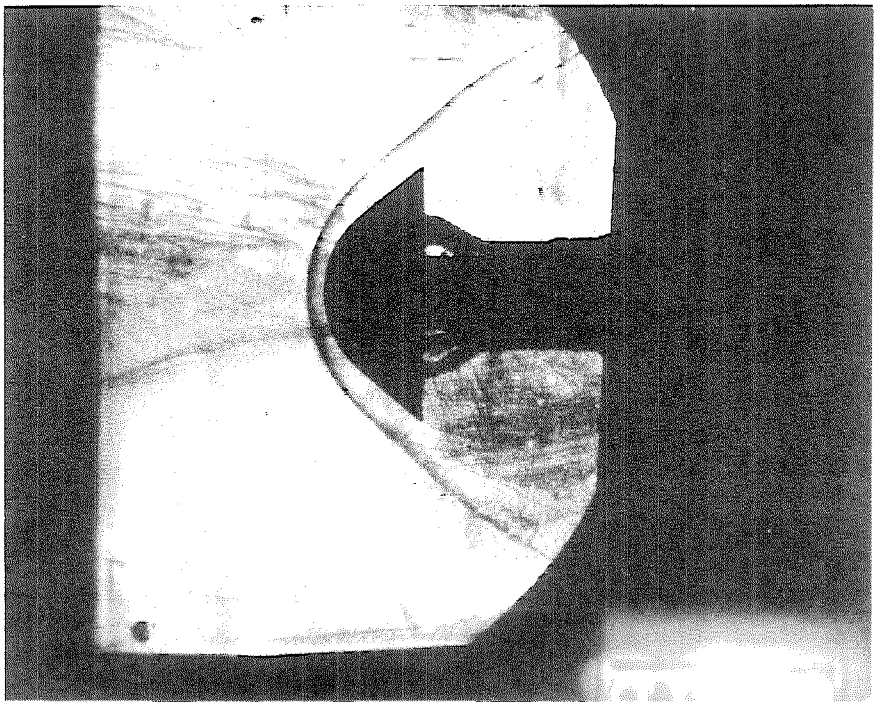

FIG. 9

SCHLIEREN PHOTOGRAPH OF 40° HALF ANGLE CONE

$r/R = 0.8$, $\alpha = 0^\circ$

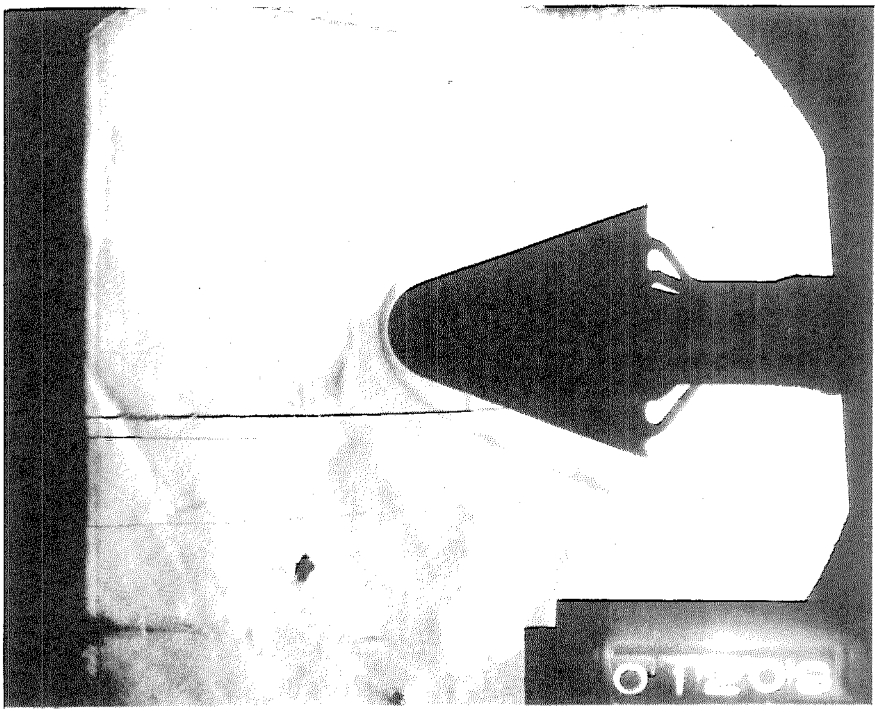

FIG. 10

SCHLIEREN PHOTOGRAPH OF 20° HALF ANGLE CONE

$r/R = 0.4,\ \alpha = 0^{\circ}$

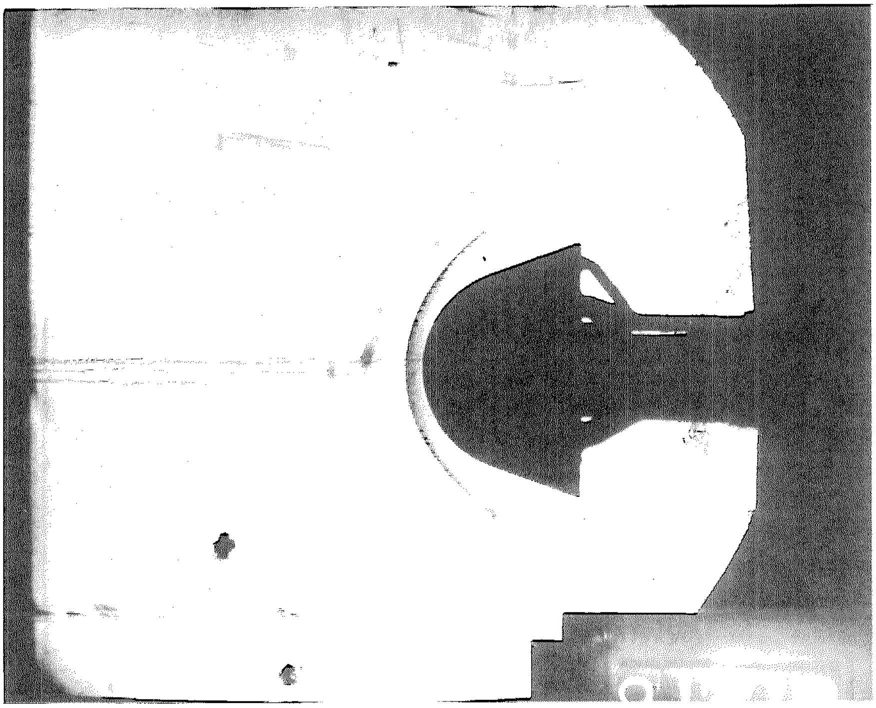

FIG. 11

SCHLIEREN PHOTOGRAPH OF 20° HALF ANGLE CONE

$r/R = 0.8,\ \alpha = 0^{\circ}$

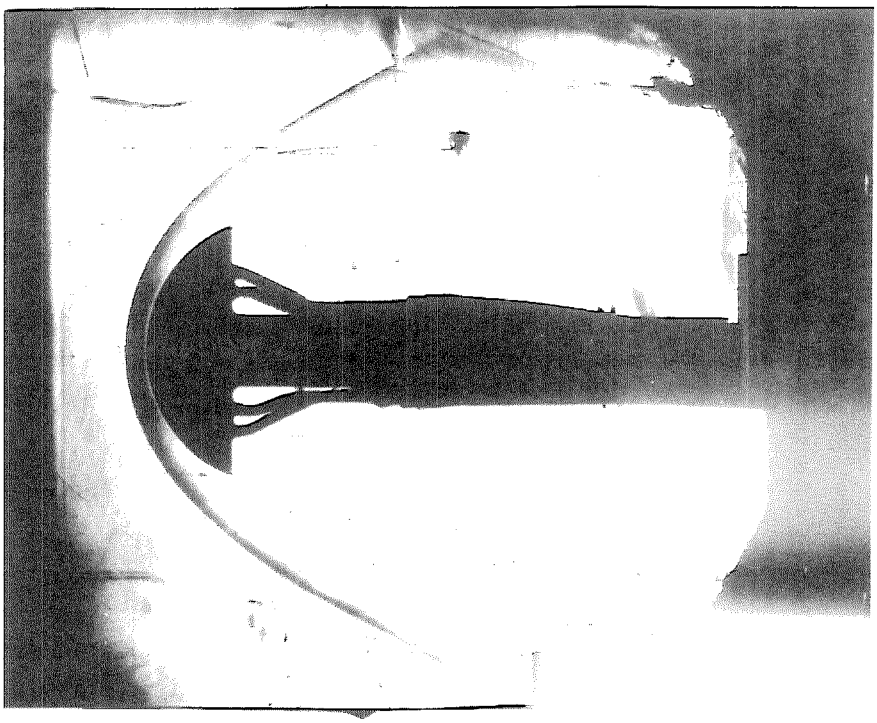

FIG. 12

SCHLIEREN PHOTOGRAPH OF 20° SPHERICAL SECTION

$r/R = 1.064$, $\alpha = 0^{\circ}$

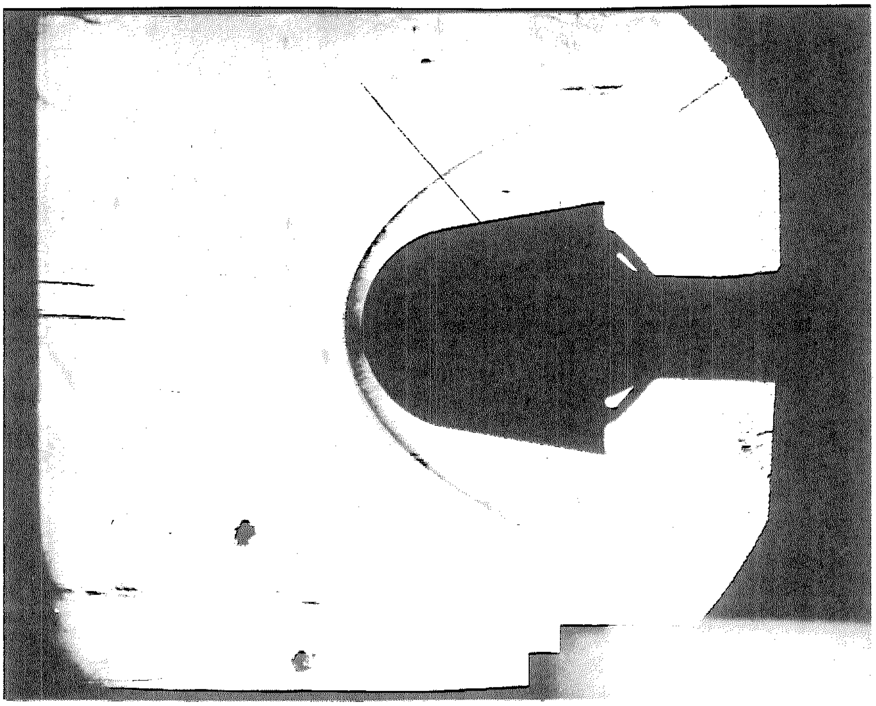

FIG. 13

SCHLIEREN PHOTOGRAPH OF 10° HALF ANGLE CONE

$r/R = 0.8$, $\alpha = 0^{\circ}$

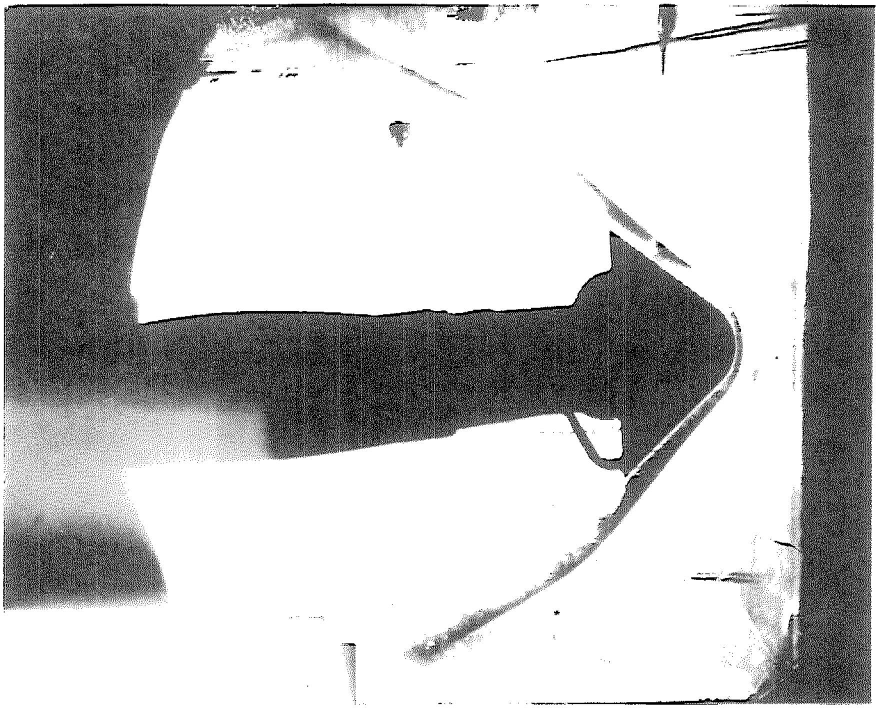

FIG. 14

SCHLIEREN PHOTOGRAPH OF 40° HALF ANGLE CONE

$r/R = 0.4, \alpha = 4^{\circ}$

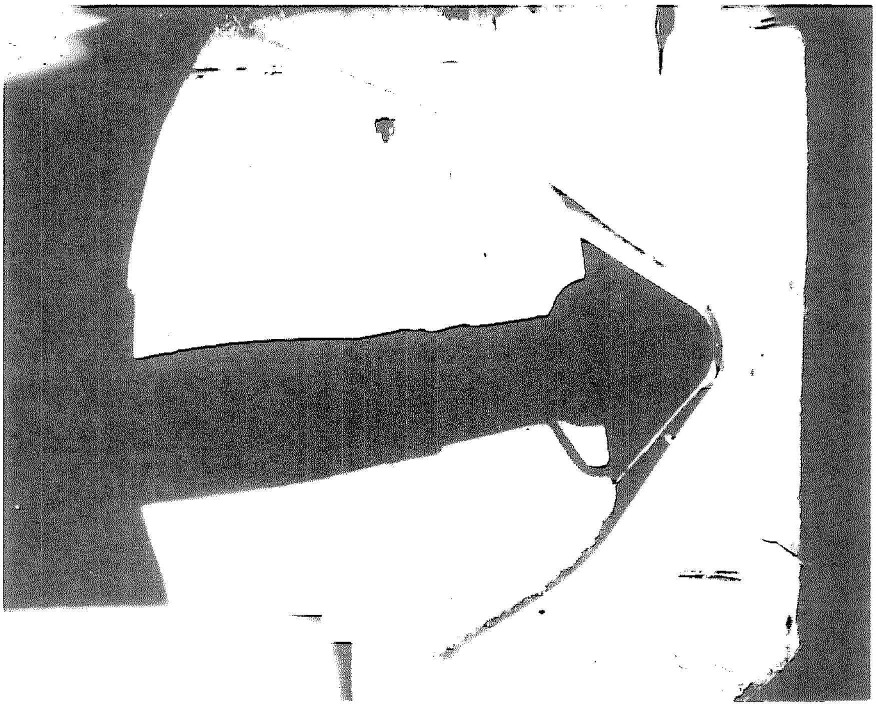

FIG. 15

SCHLIEREN PHOTOGRAPH OF 40° HALF ANGLE CONE

$r/R = 0.4, \alpha = 8^{\circ}$

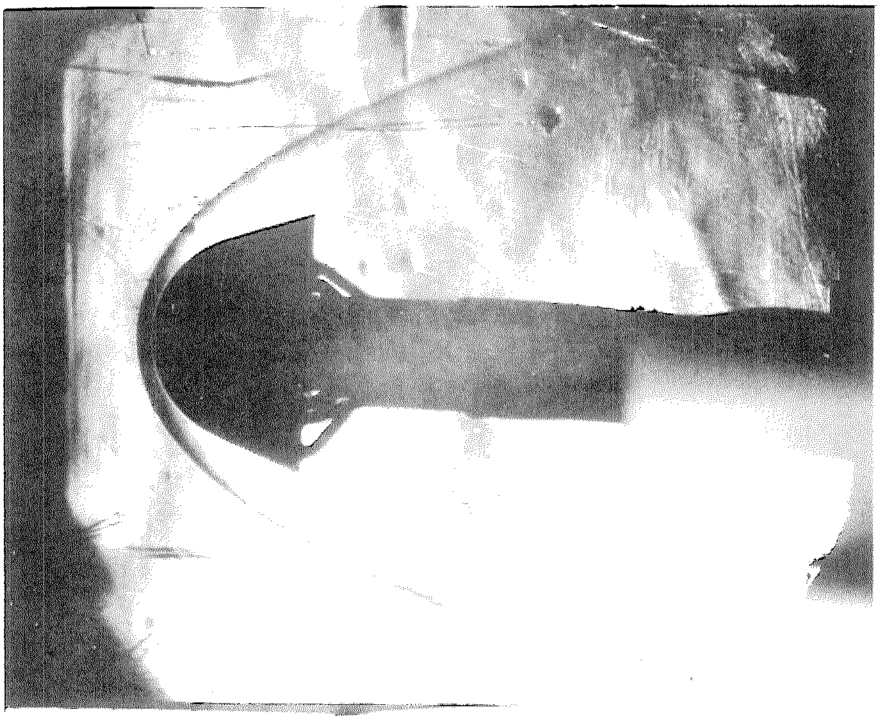

FIG. 16

SCHLIEREN PHOTOGRAPH OF 20° HALF ANGLE CONE

$r/R = 0.8, \alpha = 4^{\circ}$

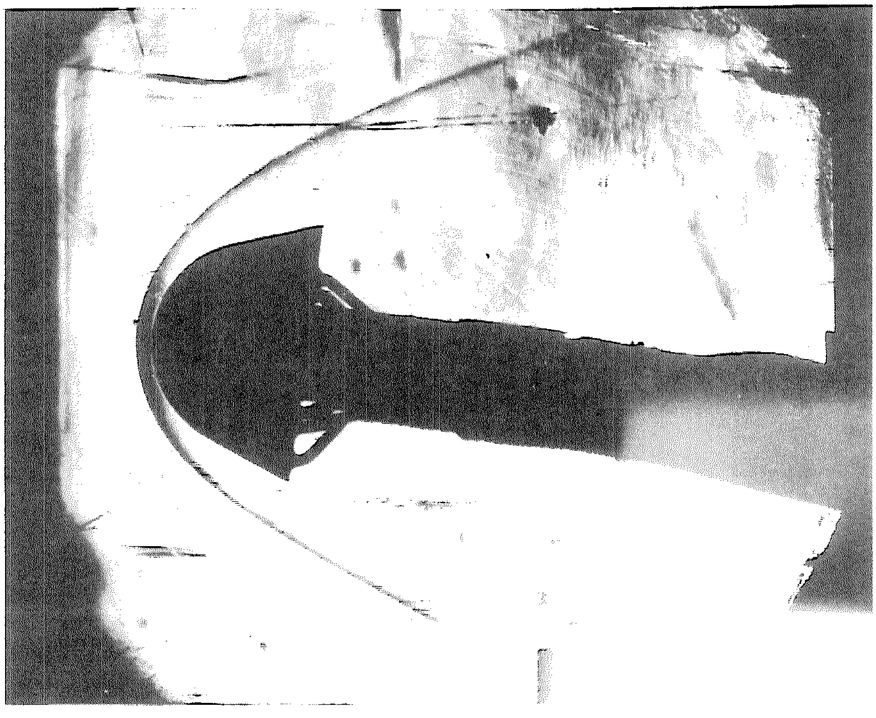

FIG. 17

SCHLIEREN PHOTOGRAPH OF 20° HALF ANGLE CONE

$r/R = 0.8, \alpha = 8^{\circ}$

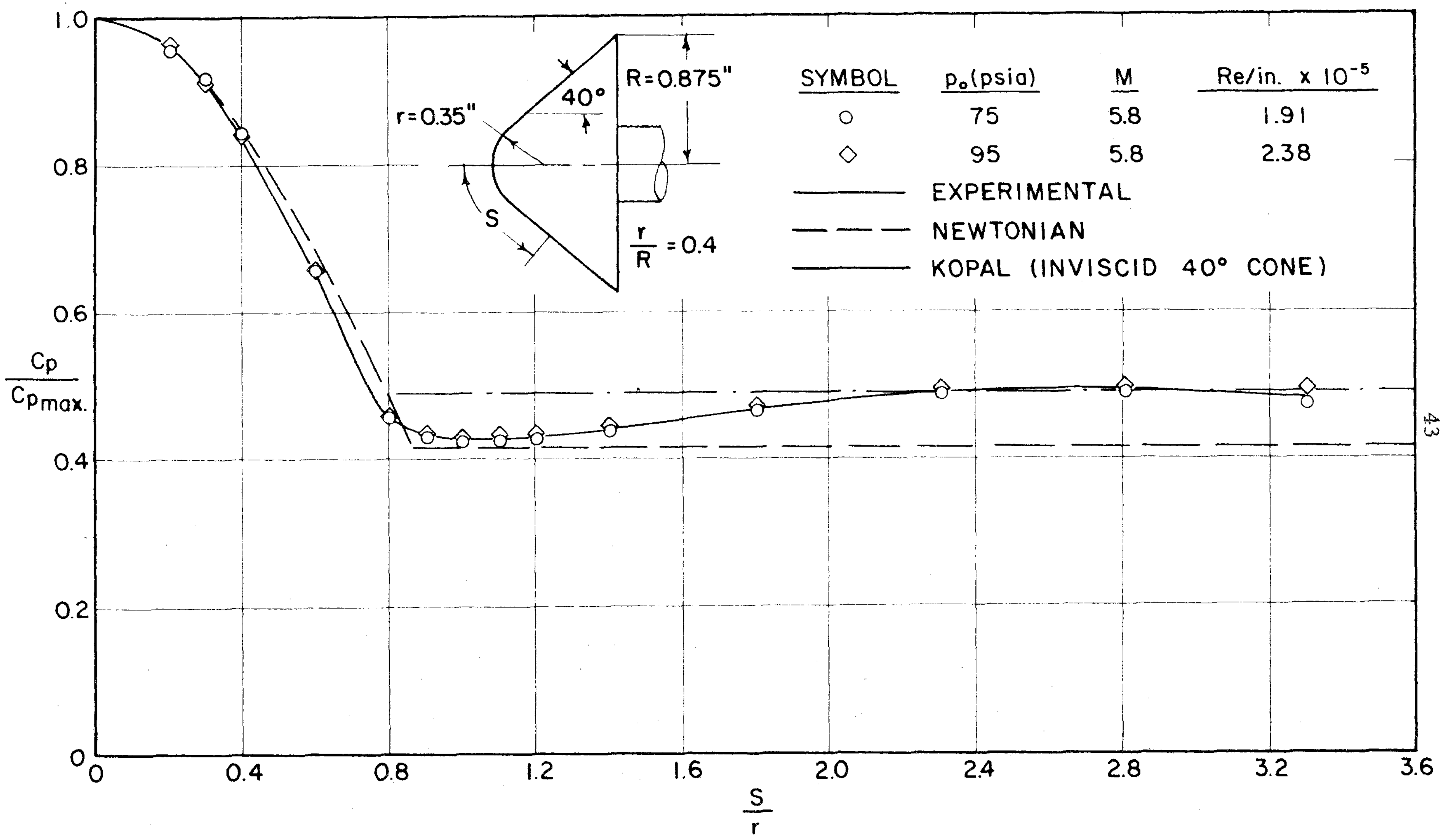

FIG. 18 SURFACE PRESSURE DISTRIBUTION, $\alpha = 0°$

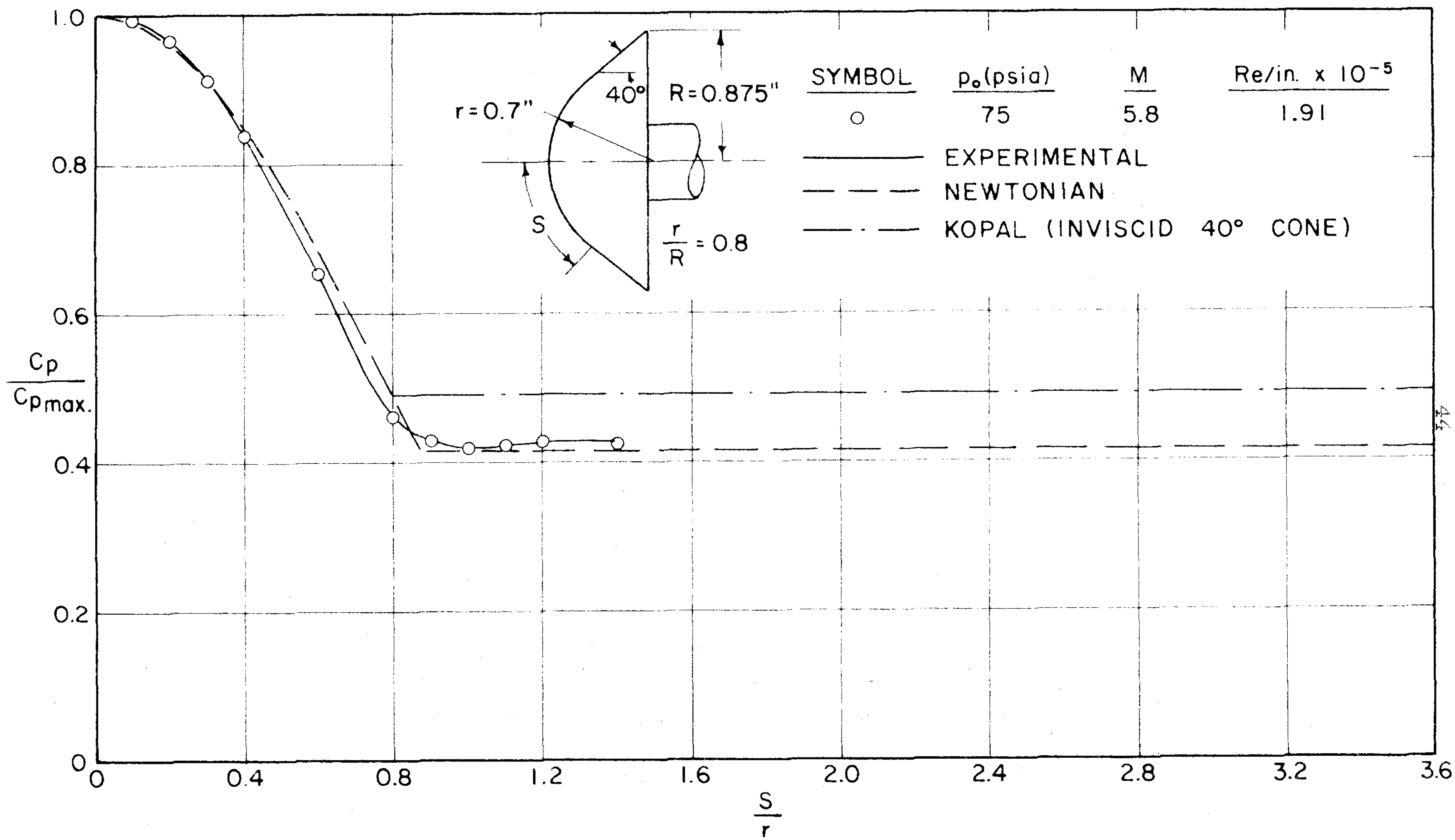

FIG. 19 SURFACE PRESSURE DISTRIBUTION, $\alpha = 0°$

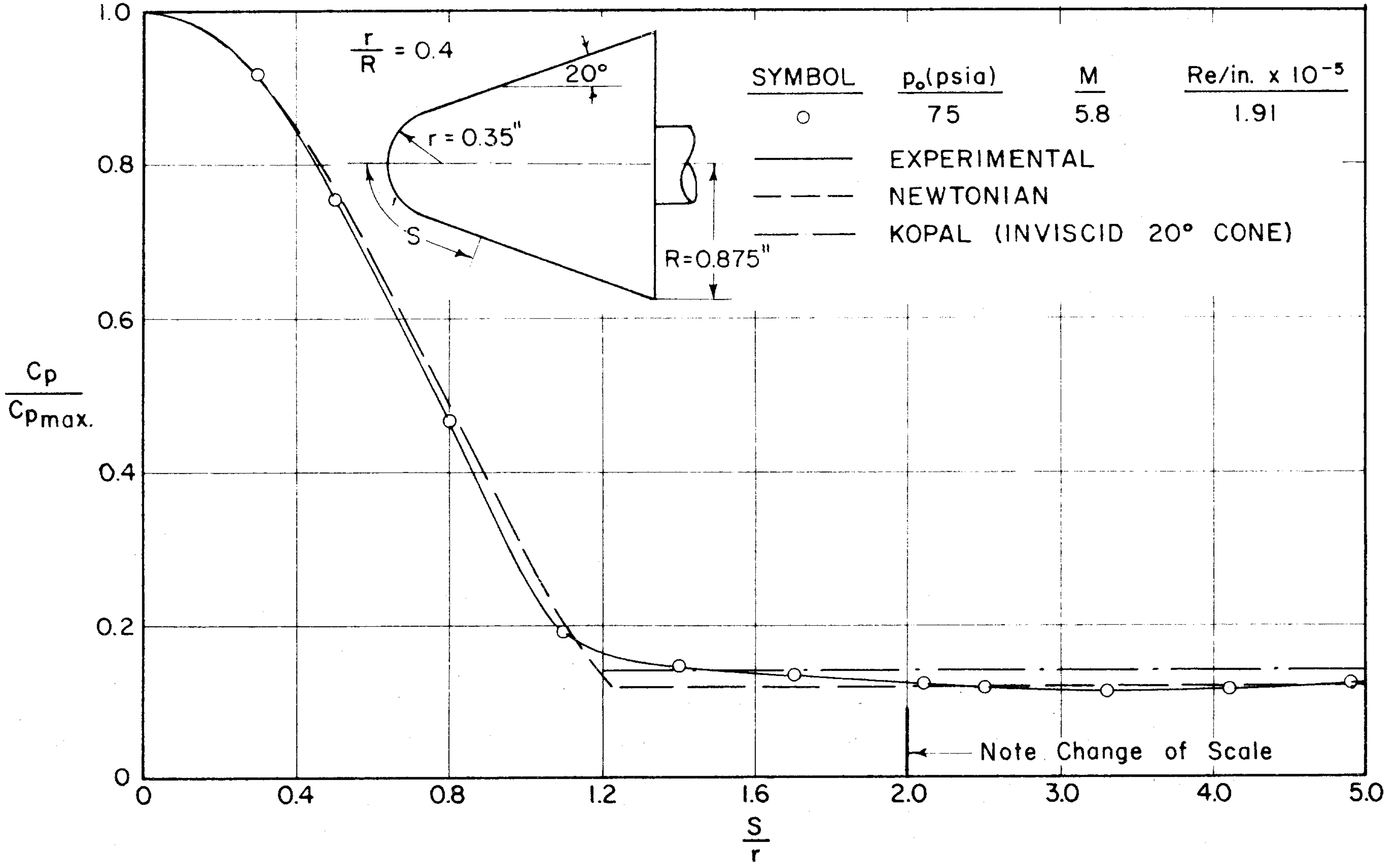

FIG. 20 SURFACE PRESSURE DISTRIBUTION, $\alpha = 0°$

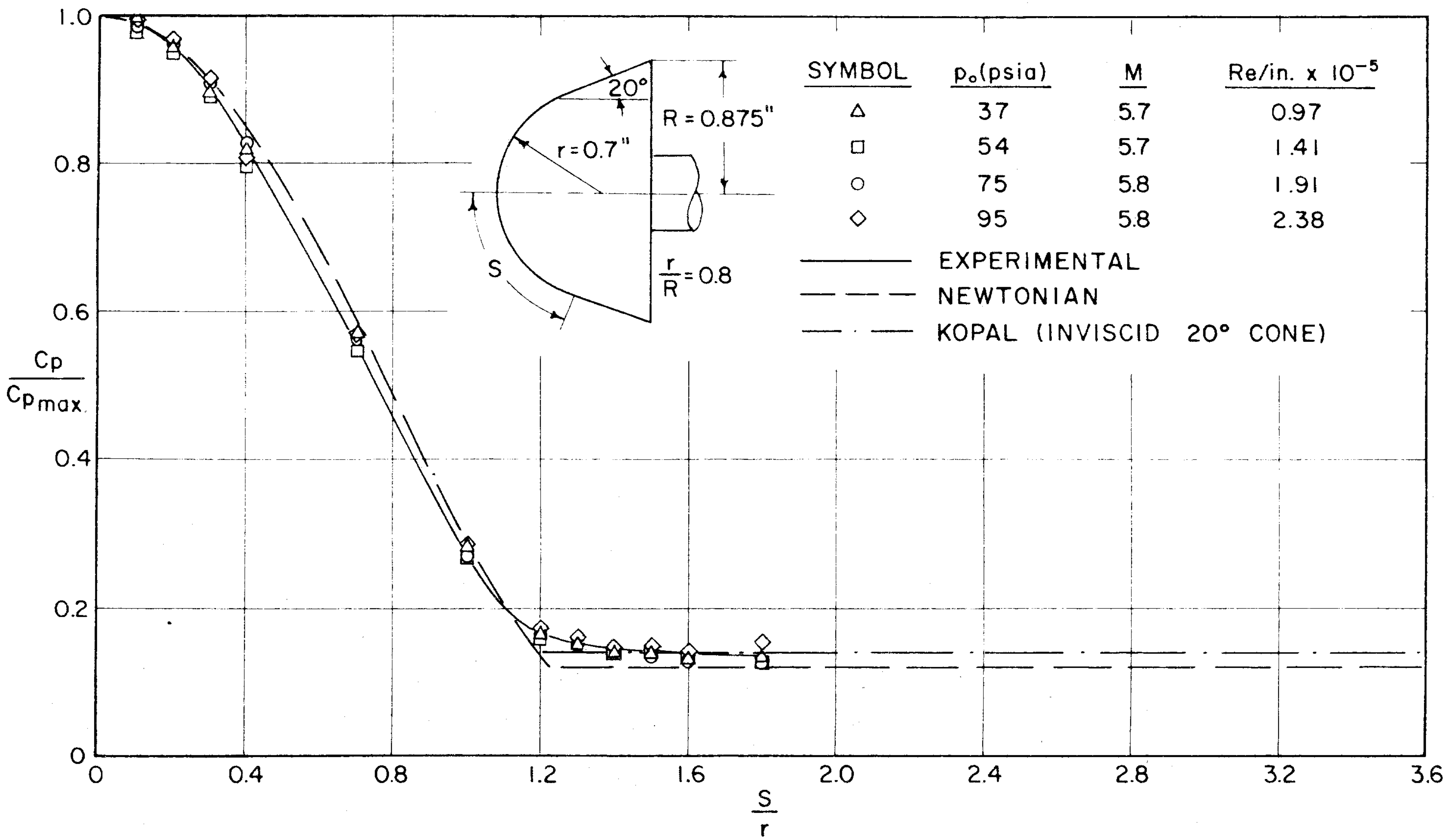

FIG. 21 SURFACE PRESSURE DISTRIBUTION, $\alpha = 0°$

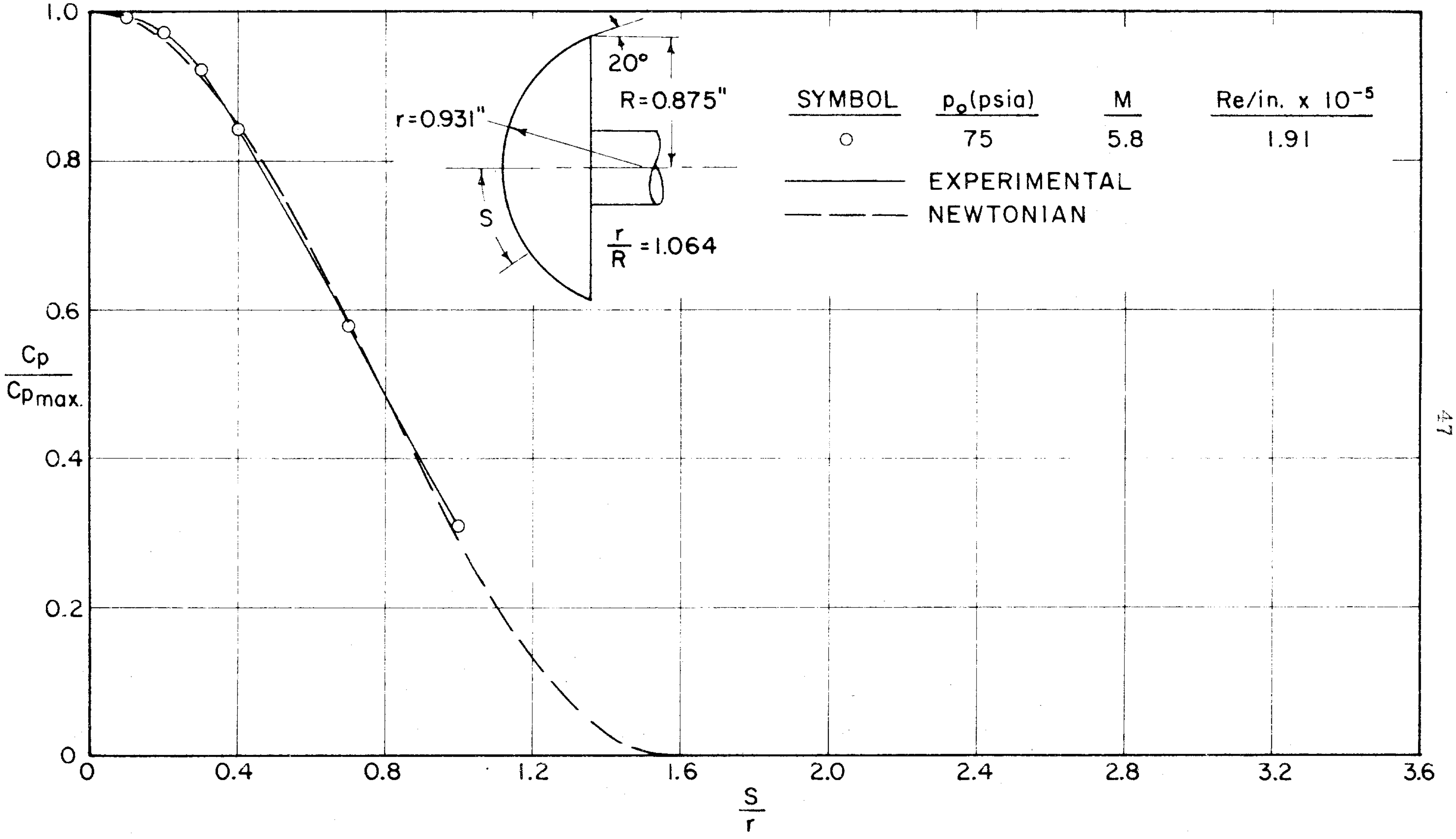

FIG. 22 SURFACE PRESSURE DISTRIBUTION, $\alpha = 0°$

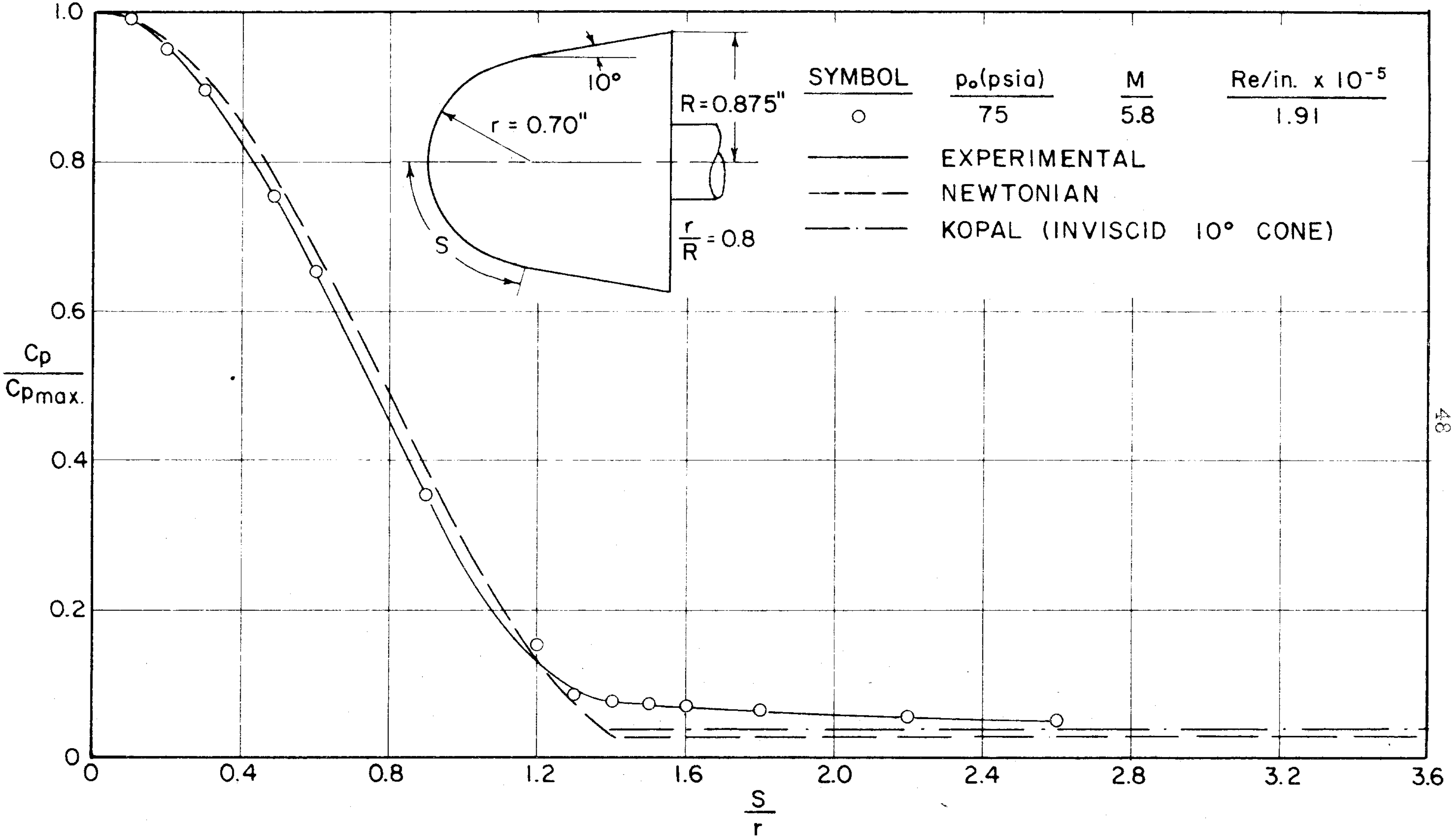

FIG. 23 SURFACE PRESSURE DISTRIBUTION, $\alpha = 0°$

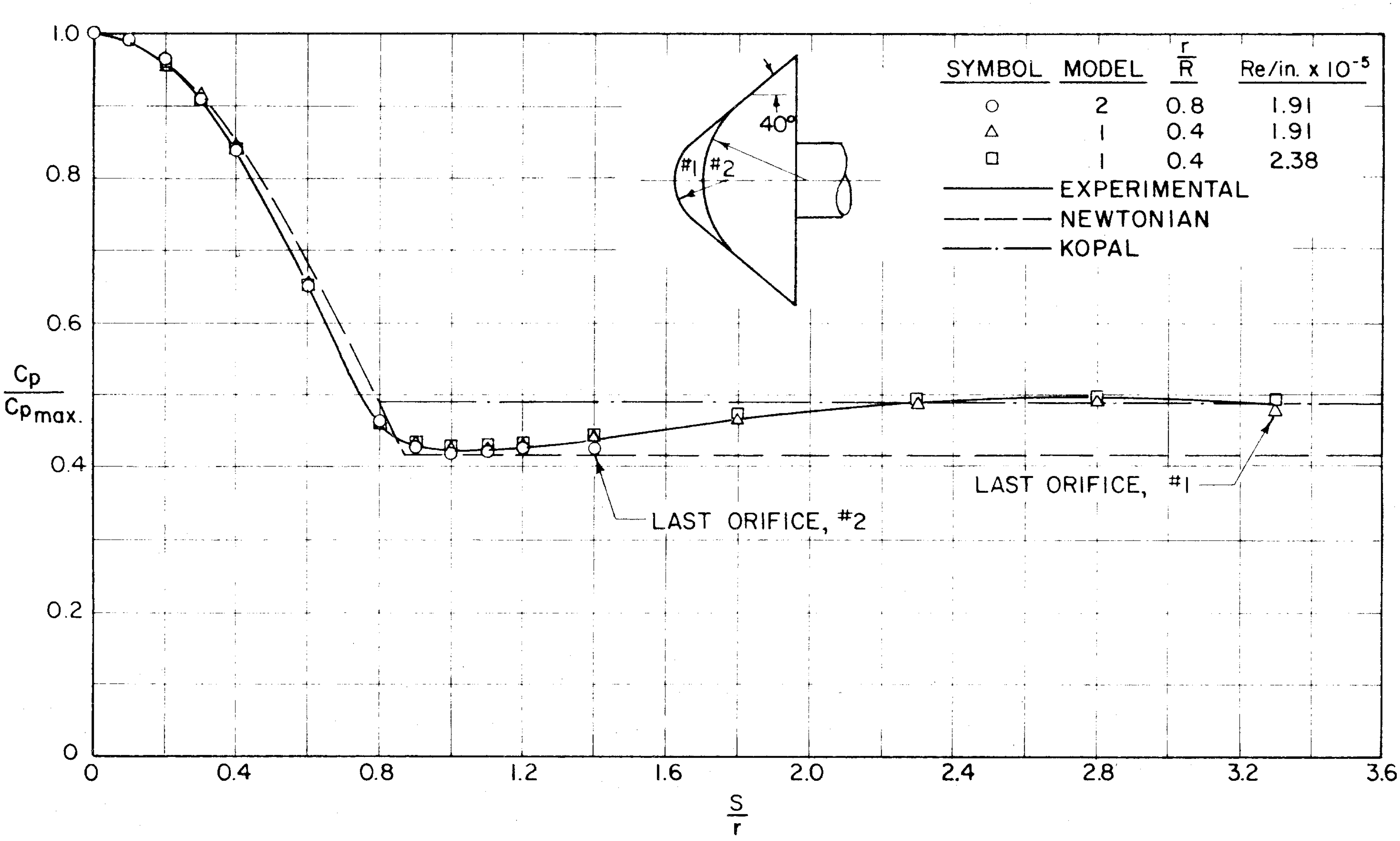

FIG. 24 SURFACE PRESSURE, $\alpha = 0°$

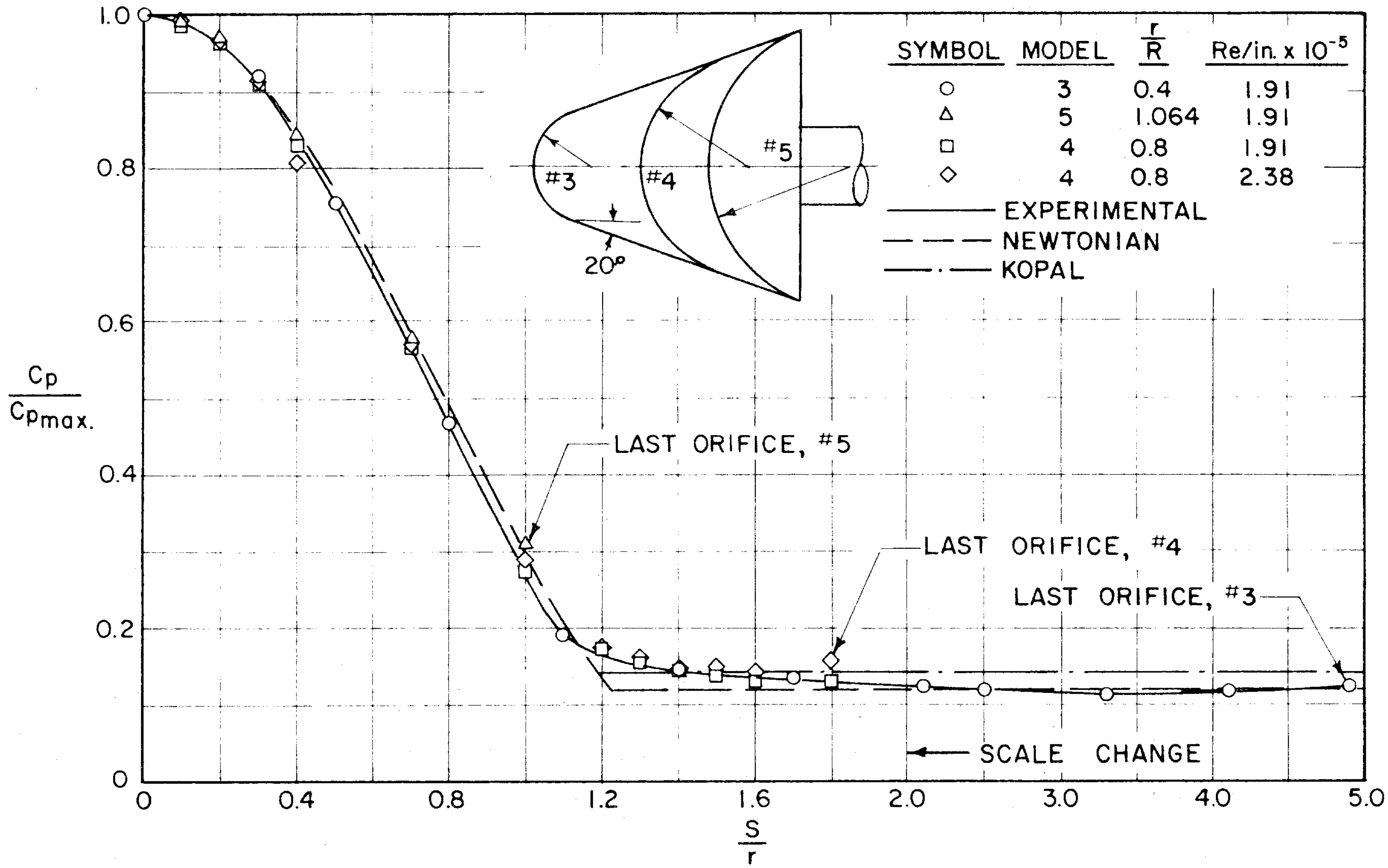

FIG. 25 SURFACE PRESSURE, α = 0°

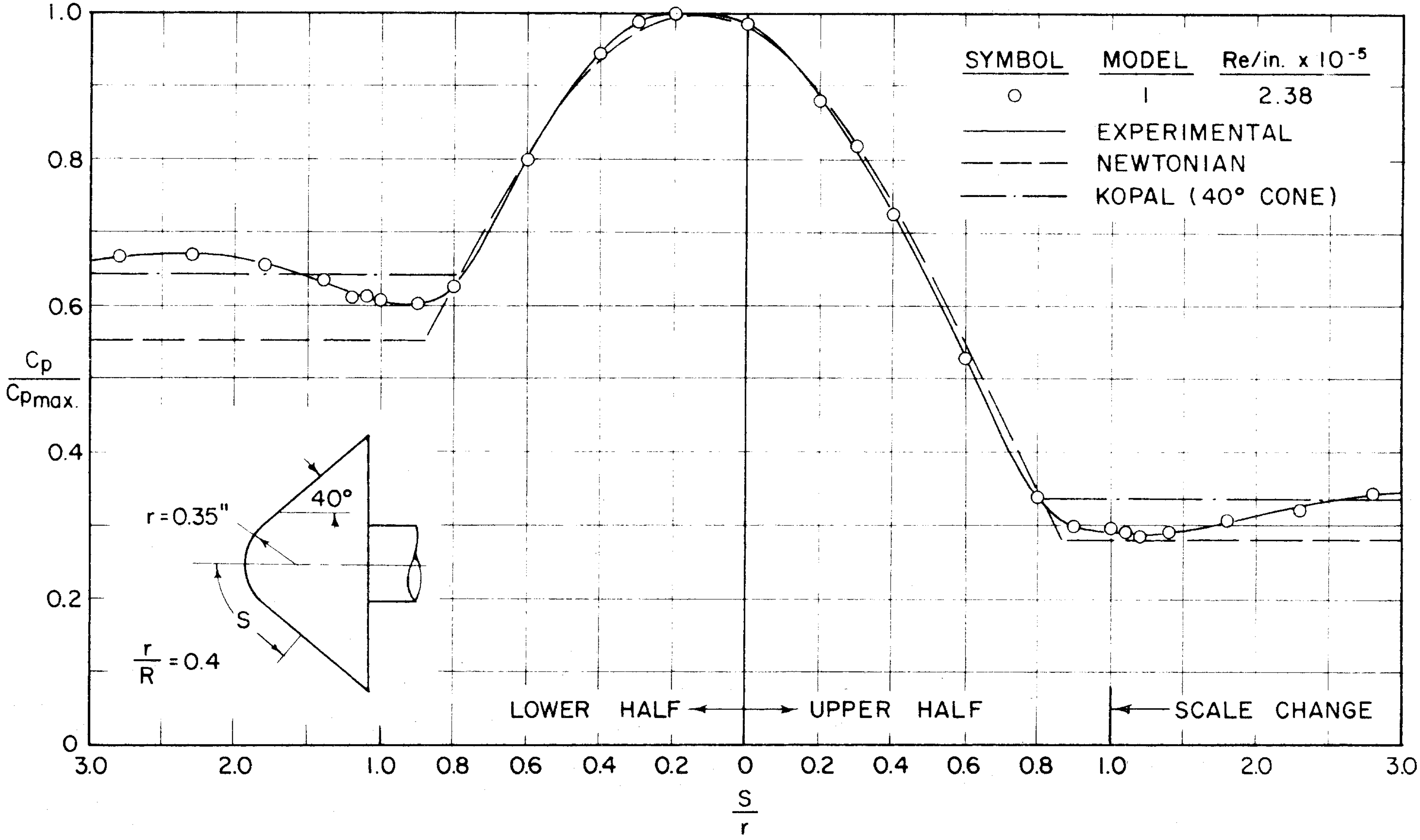

FIG. 26 SURFACE PRESSURE, VERTICAL MERIDIAN PLANE, $\alpha = 8°$

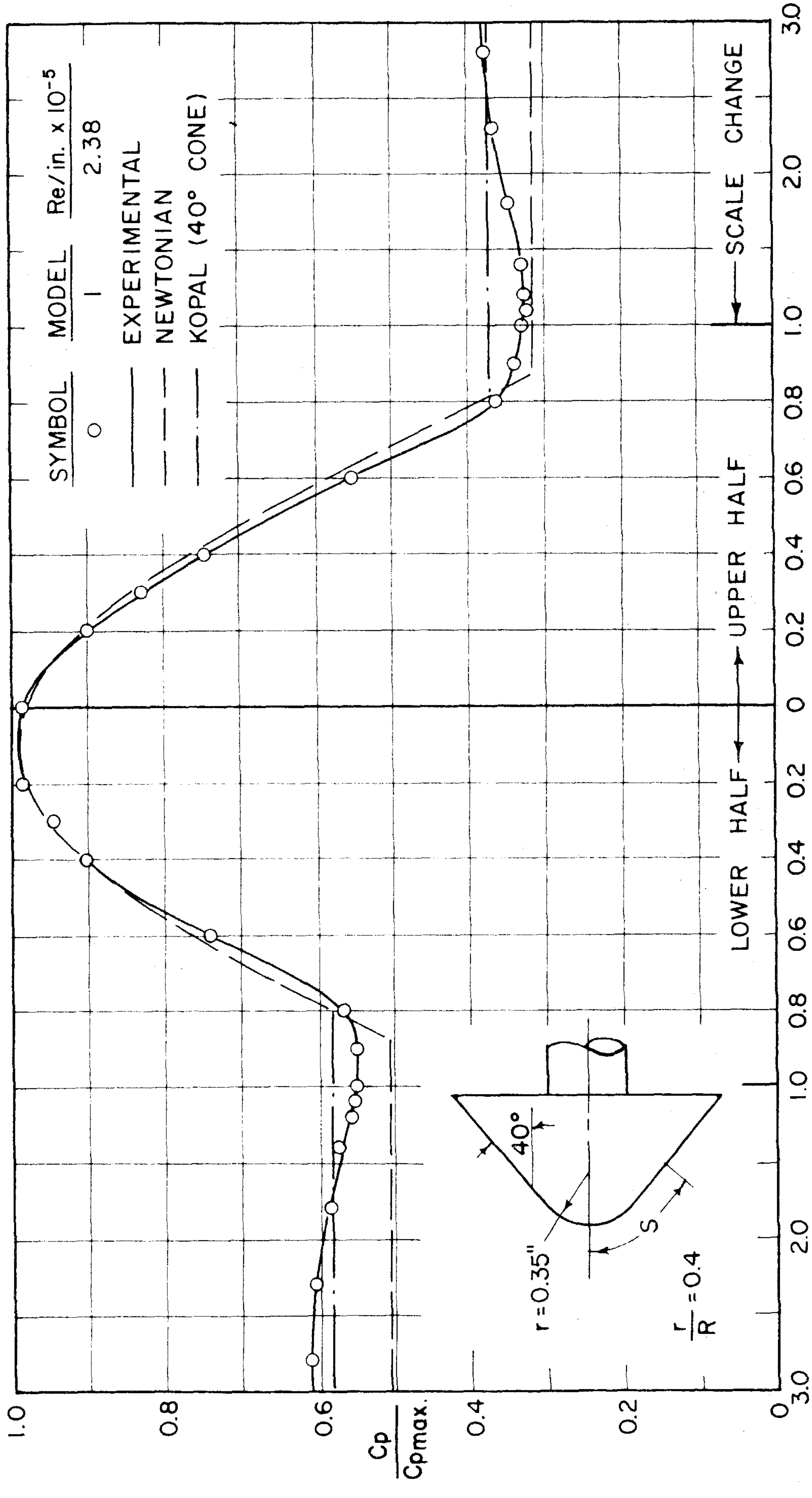

FIG. 27 SURFACE PRESSURE, DIAGONAL MERIDIAN PLANES, α = 8°

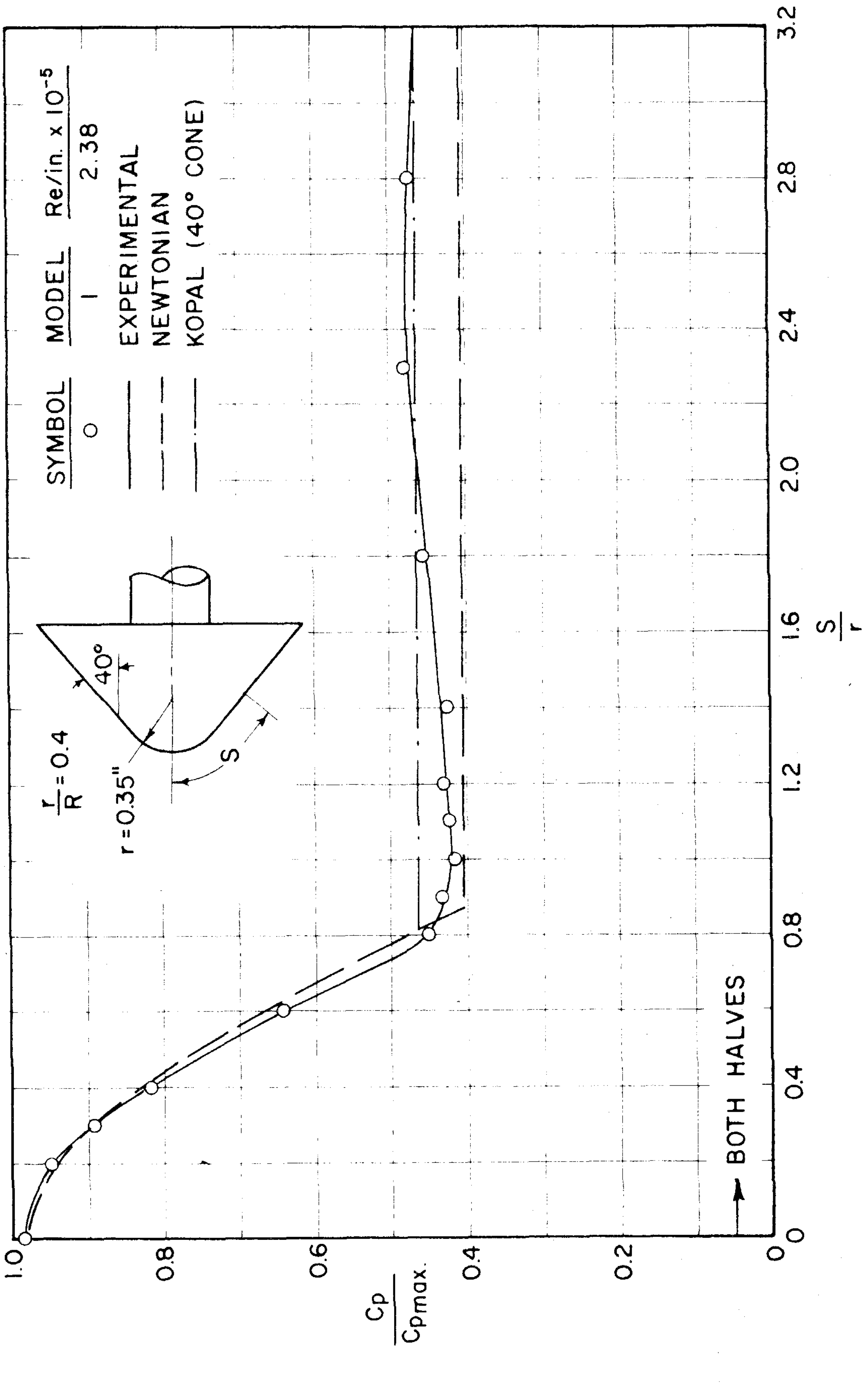

FIG. 28 SURFACE PRESSURE, HORIZONTAL MERIDIAN PLANE, $\alpha = 8°$

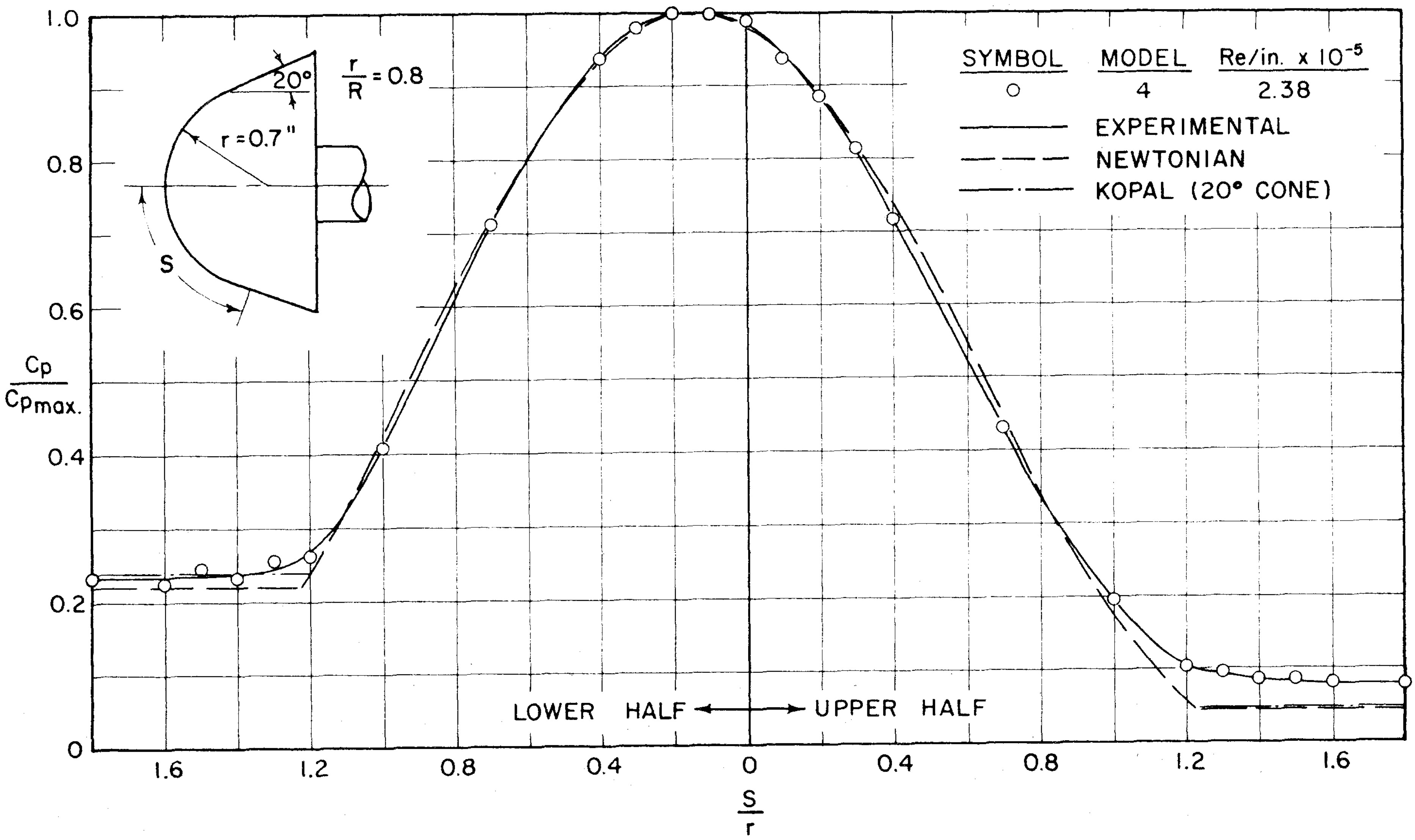

FIG. 29 SURFACE PRESSURE, VERTICAL MERIDIAN PLANE, $\alpha = 8°$

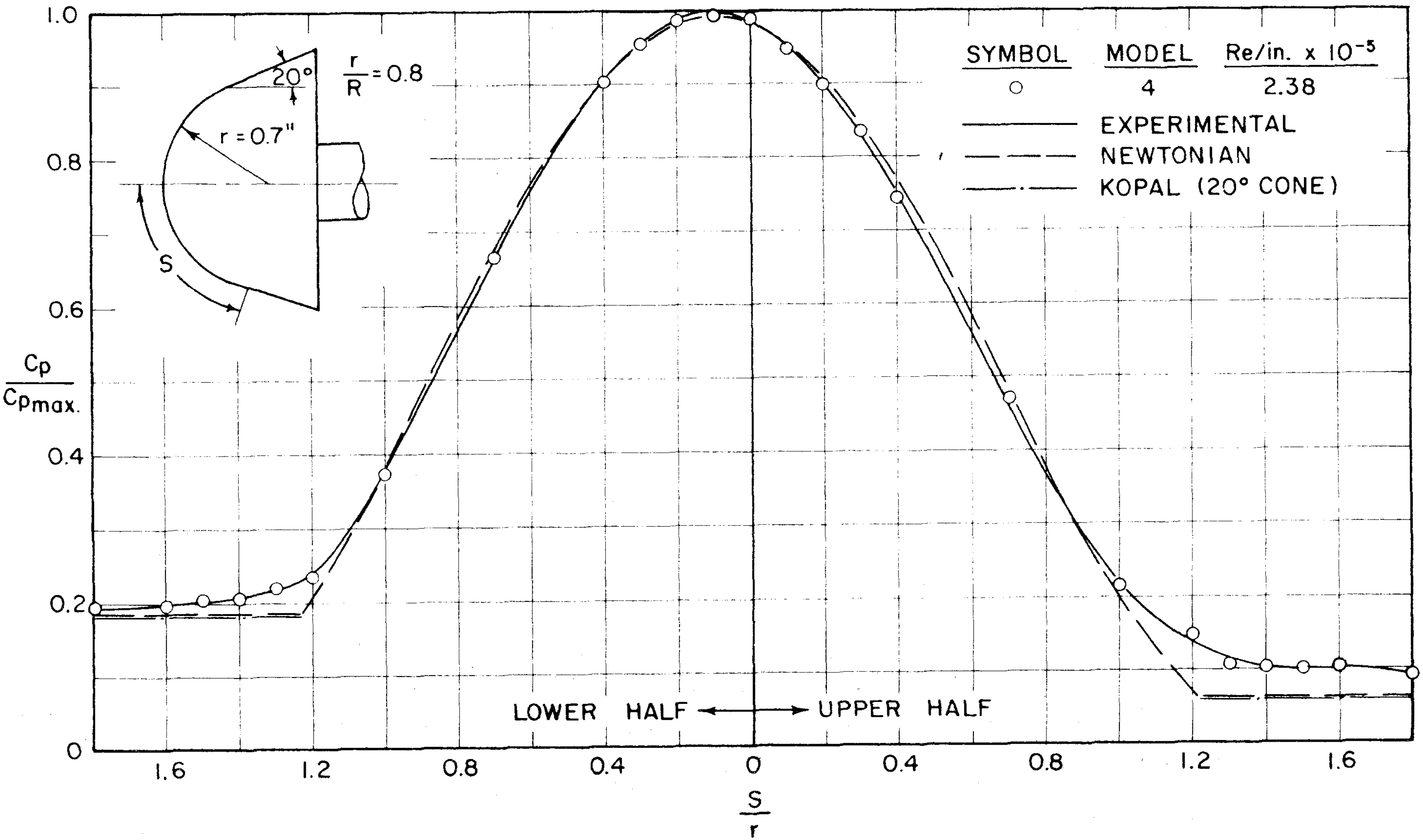

FIG. 30 SURFACE PRESSURE, DIAGONAL MERIDIAN PLANES, $\alpha = 8°$

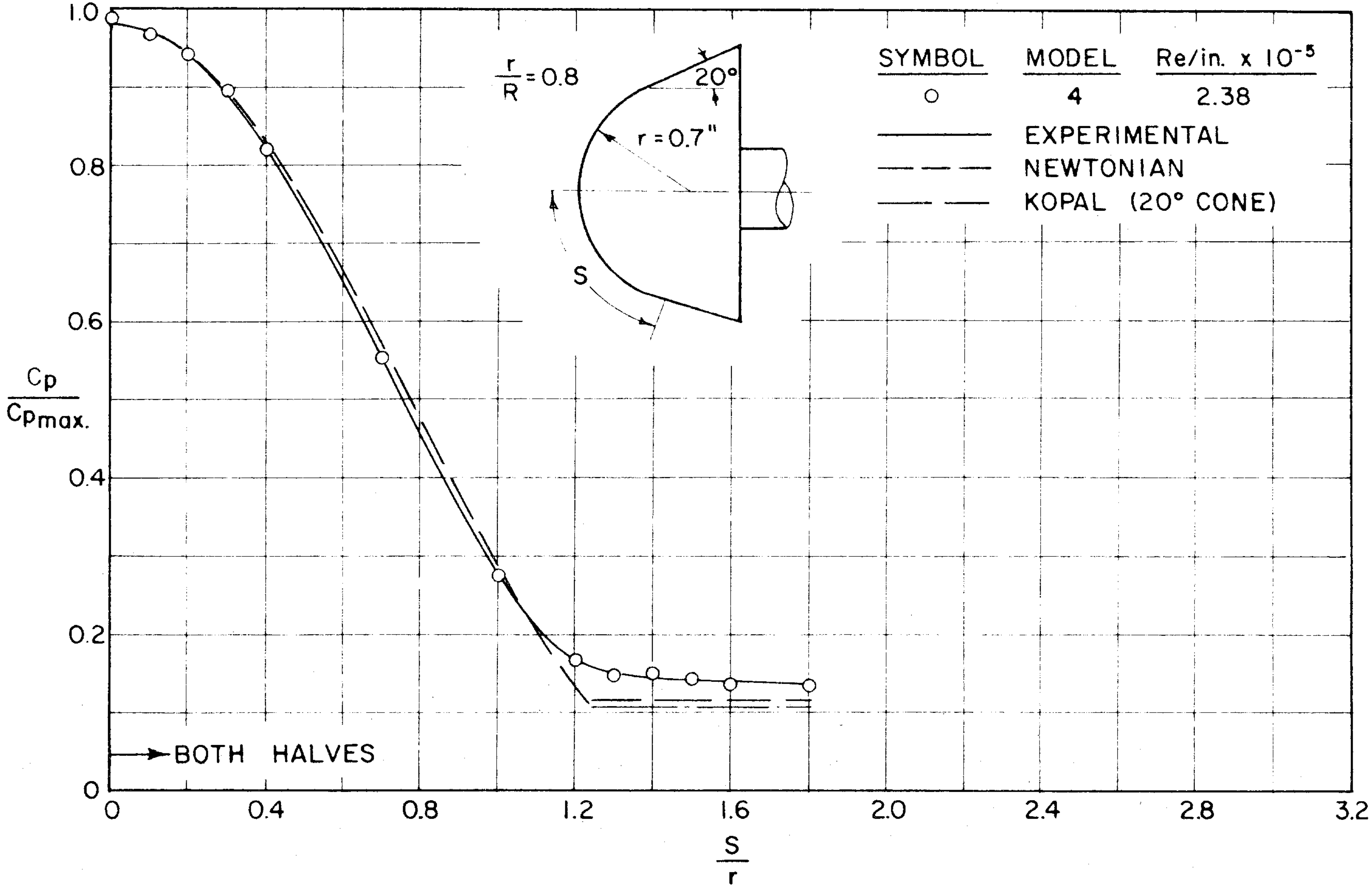

FIG. 31 SURFACE PRESSURE, HORIZONTAL MERIDIAN PLANE, $\alpha = 8°$

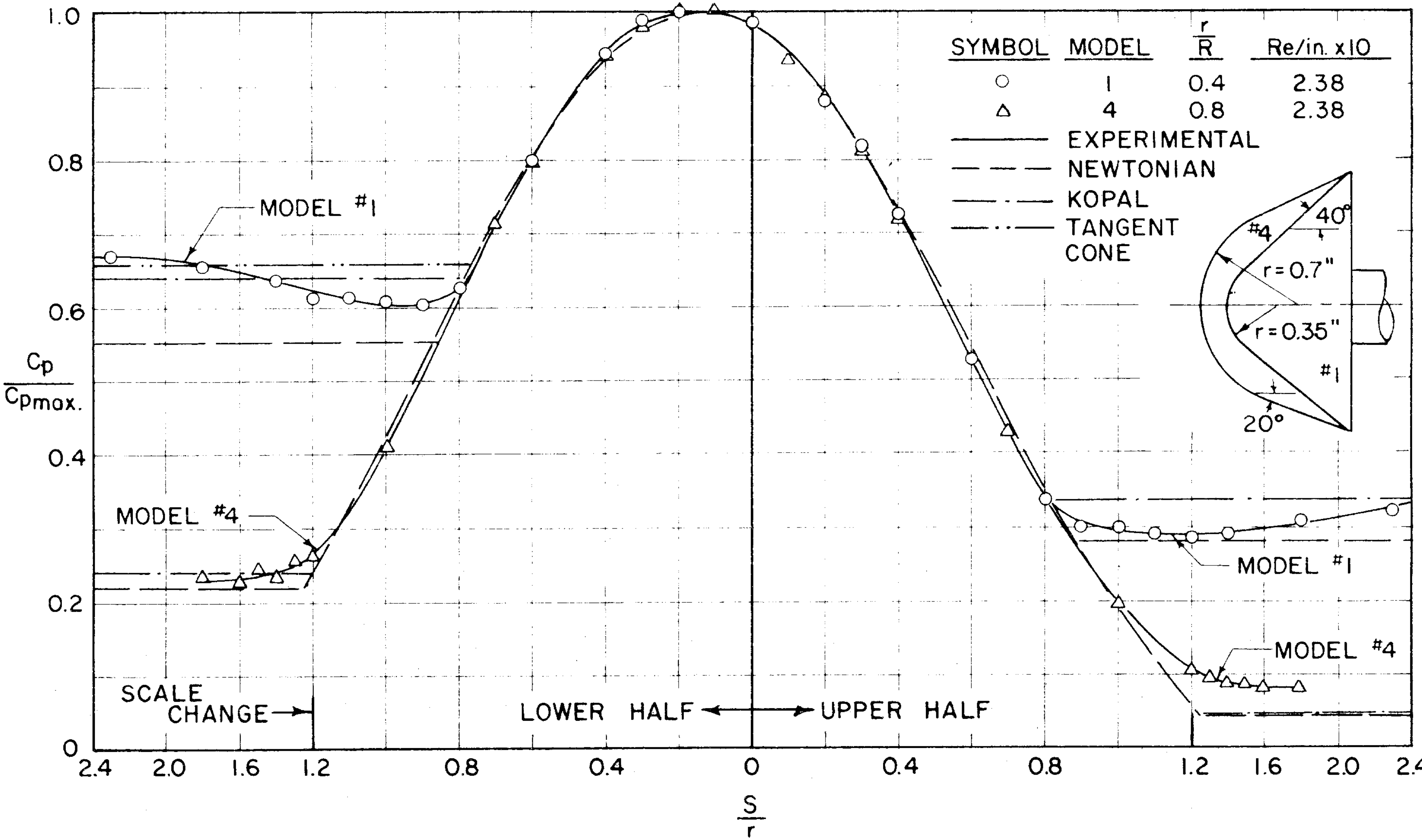

FIG. 32 SURFACE PRESSURE, VERTICAL MERIDIAN PLANE, α = 8°

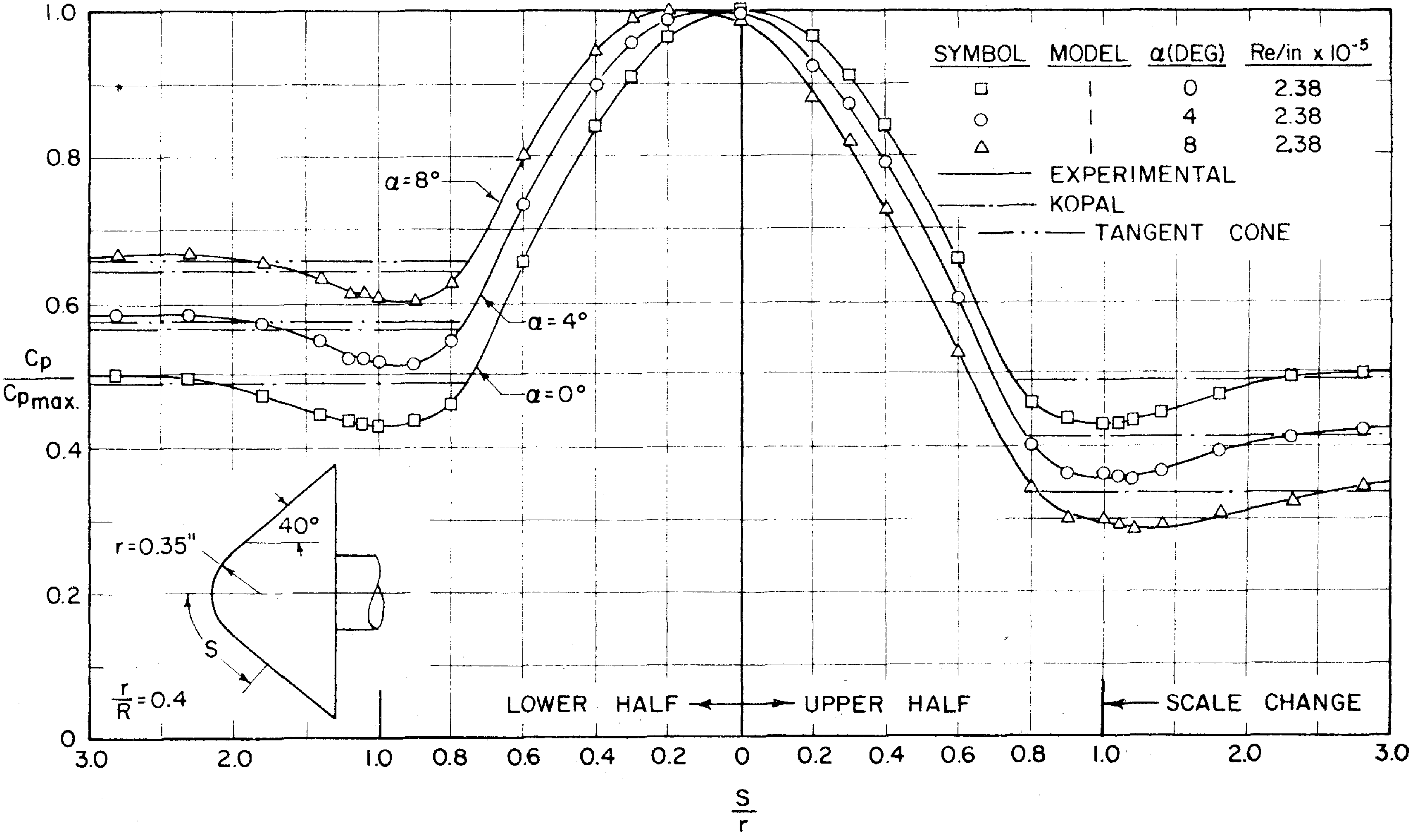

FIG. 33 SURFACE PRESSURE, VERTICAL MERIDIAN PLANE, $\alpha = 0°, 4°, 8°$

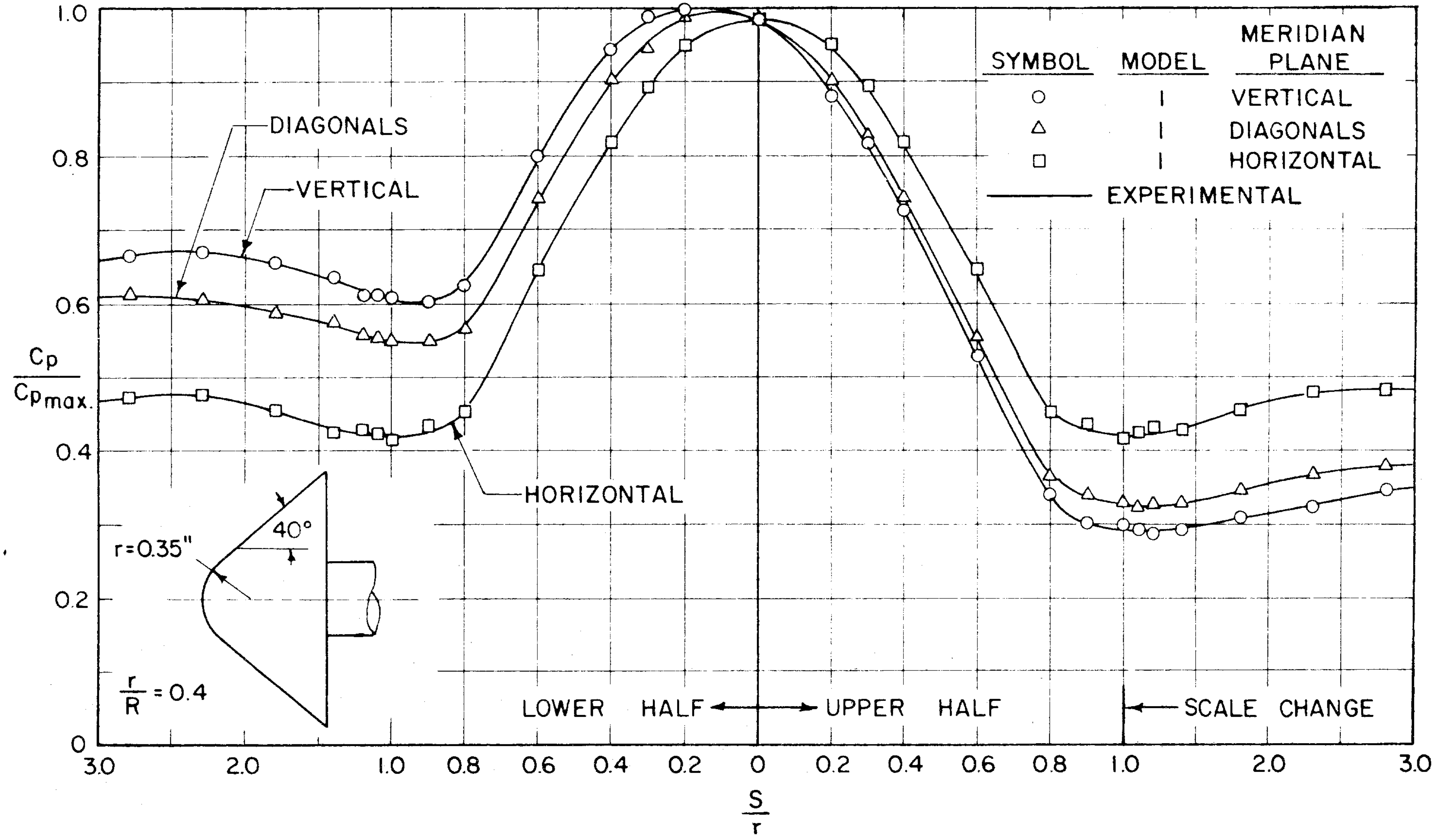

FIG. 34 SURFACE PRESSURE, FOUR MERIDIAN PLANES, $\alpha = 8°$

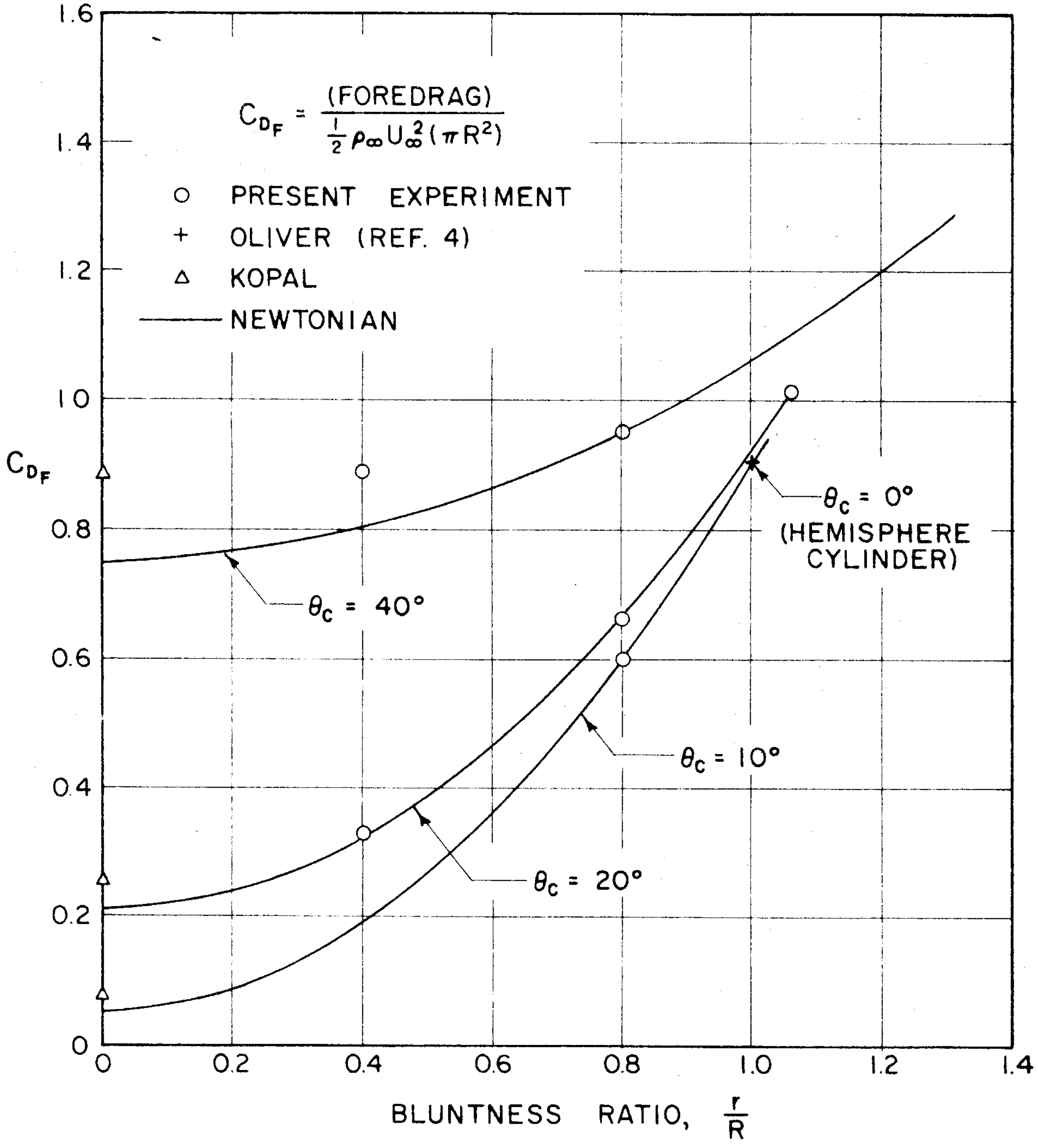

PRESSURE FOREDRAG OF SPHERICAL NOSED CONES AT MACH NUMBER 5.8

FIG. 35